Journal of Applied Fluid Mechanics, Vol. 18, No. 9, pp. 2180-2201, 2025.
Available online at www.jafmonline.net, ISSN 1735-3572, EISSN 1735-3645.
https://doi.org/10.47176/jafm.18.9.3391

Research on the Three-dimensional Transient Characteristics of the Hydraulic System during Load Rejection with Combined Regulation of Ball Valve and Guide Vanes in the Entire Hydraulic Passage of the Pumped Storage Power Stations

X. Li[1,2†], X. Tang[1,2], Q. Ren[3], Q. Liu[4], and H. An[5]

[1.] *College of Water Resources and Civil Engineering, China Agricultural University, Beijing, 100083, China*
[2.] *Beijing Engineering Research Center of Safety and Energy Saving Technology for Water Supply Network System, China Agricultural University, Beijing, 100083, China*
[3.] *CGGC International LTD., Beijing, 100000, China*
[4.] *North China University of Water Resources and Electric Power, Zhengzhou, He'nan, 450000, China*
[5.] *Worcester Polytechnic Institute, Worcester, 01609, USA*

†*Corresponding Author Email: lxq@cau.edu.cn*

ABSTRACT

The complex transient flow field in the entire hydraulic system of a large pump turbine under load rejection conditions, involving the simultaneous closing of the ball valve and guide vanes, is comprehensively investigated using the Re-Normalization Group (RNG)k-ε model and Fast Fourier Transform (FFT) technique. The predicted pressures at the volute inlet and guide vane outlet show good agreement with the field test data, with corresponding relative errors of 0.87% and 0.33%, respectively, between the predicted maximum pressures and those measured in the field. The main frequencies of pressure at the volute inlet are the unit rotating frequency during the initial time stages (0–3s), and low-frequency fluctuations in the later stages (3–8s and 8–11s). In contrast, the corresponding frequencies at the guide vane outlet are consistent with the blade frequency. During the ball valve closing process, as the unit rotational speed increases, complex flow separations cause vortices near the middle of the runner to coalesce into two large vortices of similar size. Meanwhile, the cross-sectional area of the vortex rope in the draft tube increases, and its spiral shape becomes increasingly irregular until it breaks apart. Based on the Q criterion, a series of 3D complex vortices form inside and downstream of the ball valve at the onset of the combined closing stage, intensifying as the guide vanes close. A spiral-shaped vortex rope in the draft tube extends downstream, breaking into smaller vortices after passing through the draft tube elbow, with the location of the fracture moving upstream as the flow rate decreases further.

Article History

Received January 22, 2025
Revised April 6, 2025
Accepted April 29, 2025
Available online July 5, 2025

Keywords:

Combined regulation
Load rejection
Pump turbine
Q criterion
Vortex

1. INTRODUCTION

When non-adjustable nuclear power and intermittent clean energy sources, such as wind and solar power, are integrated into the power grid, it leads to a deterioration in power grid quality. The peak-valley difference in the grid becomes larger, resulting in imbalance of power distribution. As an effective solution to these challenges, pumped storage power stations (PSPSs) are becoming increasingly important due to their large unit capacity, strong peak shaving and valley filling performance (Zhang et al., 2024), especially for units with high water head, large capacity, large water head changes, and quick power-grid connection performance (Jurasz & Mikulik, 2017; Zeng et al., 2017; Hoffstaedt et al., 2022). Frequent switching of operating conditions in pump-turbine units, such as load rejection, switching between pump and turbine modes, start-up and shutdown processes, and power regulation (Yang et al., 2020; Fu et al., 2023), as well as the S-shaped performance of the unit (Widmer et al., 2011), can lead to a series of complex transient characteristics in the hydraulic system. These characteristics can negatively affect the operational and safety performance of the unit, potentially causing unit vibration, difficulties in grid connection, and even accidents (Zhang et al., 2016).

NOMENCLATURE

1D	One-dimensional	Δ	one of criteria to identify vortices
3D	Three-dimensional	Ω	antisymmetric tensor
CFD	Computational Fluid Dynamics	a_ε	model constant
DES	Detached Eddy Simulation	a_k	model constant
DM	Dynamic Mesh Model	C_μ	model constant
FFT	Fast Fourier Transform	det	value of the determinant matrix
MOC	Method of Characteristic	f_i	quality force
MRF	Multiple Reference Frame	G_k	turbulent-kinetic-energy generation term
N-S	Navier-Stokes	k	turbulent kinetic energy
PSPS	Pumped Storage Power Station	p	transient pressure
PT	Pump Turbine	Q	one of criteria to identify vortices
RSM	Reynolds Stress Model	R	additional term
SM	Sliding Mesh	S	symmetric tensor
VOF	Volume of Fluid	t	time
β	model constant	tr	trace of the matrix
ε	dissipation rate per unit volume	u_i	components of the flow velocity
η_0	model constant	X	Galilean invariant
λ_2	one of criteria to identify vortices	x_i	coordinate components
μ_t	eddy viscosity	Y	Galilean invariant
ρ	density	Z	Galilean invariant

In all transient processes where changes and fluctuations in unit rotating speed and pressure in the hydraulic system are more pronounced, full-load rejection is the most dangerous, especially for high head and large-flow-rate units (Chen et al., 2020; He et al., 2023). A reasonable guide vane adjustment rule for flow rate control is an economical and effective method to improve transient characteristics, and it has been applied in many hydropower stations (Li et al., 2018). However, for PSPSs with large variations in high water heads, this regulation technology cannot meet the required performance standards. Therefore, the combined regulation of flow rate using both the ball valve and guide vanes can effectively improve transient characteristics, thus meeting the regulation performance requirements. However, this approach introduces more complex internal transient flow in the hydraulic system, and there is relatively little research on the underlying mechanisms.

The dynamic characteristics of the pump turbine (PT) during the transient process differ significantly from the static characteristics under steady-state conditions (Walseth et al., 2016). Currently, there are three numerical methods used to study the transient characteristics of hydropower stations: one-dimensional (1D), three-dimensional (3D) computational fluid dynamics (CFD), and 1D-3D coupling methods.

The 1D method of characteristic (MOC) is the most widely used numerical method for hydraulic transient analysis in hydropower stations (Zeng et al., 2015; Vakil & Firouzabadi, 2019). This method is capable of obtaining pressure and flow rate changes in hydraulic systems, as well as the unit's rotating speed variations, due to its mature theory, high computational efficiency, stable calculations, and ability to handle complex boundary conditions. It also considers different friction models and variable wave velocities (Guo et al., 2020; Zheng et al., 2020).

Zhang et al. (2020) proposed a dynamic model for the multi-unit hydraulic system of a PSPS. This model accounted for the coupling effects among units during the transient process, integrated the hydraulic system with the pump-turbine system, and further studied the dynamic response characteristics of two units in the same headrace tunnel when one unit rejects full load under three different guide-vane closing laws. The results indicated that the timing of the turning point of the guide-vane opening reflected the sudden change in turbine flow and was a critical factor for adjusting the transient characteristics during load rejection conditions. The head fluctuation of the unit rejecting load was consistently higher than that of the non-load-rejecting unit, with similar fluctuation periods.

Based on 1D MOC and modified Suter transformations, Rezghi & Riasi (2016) analyzed the influence of the unit's moment of inertia and the head-loss coefficient of the surge-tank connection pipe on numerical hydraulic transient parameters under runaway conditions during the simultaneous operation of two units at the Siah Bishe power plant. The plant has two parallel pump-turbine units sharing a common headrace tunnel. The results showed that increasing the moment of inertia could delay the maxima of pressure and rotating speed, while the head-loss coefficient of the surge-tank tunnel had a significant impact on the maximum water level of the surge tank and the maximum torque of the unit.

Chen et al. (2019) systematically investigated the effects of pipe geometrical parameters on the maximum pressure during simultaneous and two-stage load rejection processes of two PTs sharing a common headrace tunnel in a PSPS. Their study concluded that the maximum pressure was closely related to the geometric characteristics of the hydraulic system, including the length and diameter of both the main and branch pipes. These parameters determine the water inertia time constant of the hydraulic system, which influences the distribution of water hammer pressure in the branch pipelines. Additionally, the ratio of the water inertia time constant in the branch pipe to that in the main pipe can be used to estimate the transient extreme pressure in the hydraulic system.

So far, the 1D MOC method has achieved significant success in engineering applications, providing valuable

guidance for controlling the maximum pressure and maximum rotating speed in practical hydraulic systems. However, it cannot capture the internal characteristics of the flow field, particularly for complex boundaries such as turbines, guide vanes, volutes, surge tanks, draft tubes and valves. Additionally, while the static performance of water turbines is used to study the transient characteristics of hydraulic systems, their instantaneous dynamic performance cannot be considered. The 1D-3D coupling method effectively addresses these limitations, with 3D CFD being employed to simulate the complex components, while 1D modeling is used for simpler hydraulic components and long pipelines (Sharon, 2020).

Based on the 1D-3D coupling method, Liu et al. (2021) studied the pressure-pulsation mechanism under the operating condition of two PTs simultaneously rejecting load in an ultra-high head pumped storage plant with two parallel pump-turbine units sharing a common headrace tunnel. The results indicated that the maximum pressure and the longest duration of overpressure exceeding industrial standards occurred in the bladeless area, due to the high pressure gradient caused by the significant reverse flow radial velocity at the inlet of the runner.

Fu et al. (2021) proposed a 1D-3D coupling method to investigate the transient characteristics under load rejection conditions for a PSPS with a hydraulic system consisting of two parallel PTs in a shared water penstock and tailrace tunnel. They further analyzed the transient variations in rotational speed, pressure, and hydraulic thrust, and identified the backflow in the runner as the cause of pressure and hydraulic thrust fluctuations. Yin et al. (2021) applied the 1D-3D coupling method to study the transient characteristics under load rejection conditions for a pump-turbine unit. The results were compared with experimental data for verification. Additionally, they proposed a boundary condition suitable for the branching junction, which was applied to the simultaneous load rejection of two units. The findings revealed that the larger water hammer pressure and the increase in unit rotational speed during the simultaneous load rejection of both units resulted in greater pressure pulsations, which, in turn, caused severe flow separation and vortices inside the runner.

Based on the 1D-3D coupling method, the pressure variations within pipes and the rotational speed of the unit can be obtained, allowing for the capture of internal flow characteristics in complex components (Feng et al., 2024). However, the treatment of 1D-3D data transmission at the coupling interface is relatively complex and cannot accurately and effectively convert 1D data into 3D data. This limitation can lead to divergence and poor stability (Zhang & Cheng 2012). Additionally, the internal characteristics of the 3D flow fields across the entire hydraulic passage cannot be fully captured.

With the rapid development of computer technology, 3D CFD techniques have been increasingly utilized to obtain detailed characteristics of internal pressure, flow velocity, and vortices in complex hydraulic systems during transient processes.

Zhou et al. (2024), based on an improved variational mode decomposition method and a multi-level wavelet denoising technique, proposed a method to accurately analyze the transient characteristics of pressure signals under load rejection conditions. This method was applied to process the pressure signals at the inlets of the volute and draft tube of a pump-turbine. The results demonstrated that the method can accurately extract both the water hammer pressure and the pulsating pressure.

Based on wall sliding mesh (SM) technology and the detached eddy simulation (DES) model, Mao et al. (2022) numerically investigated the transient characteristics of the unit section, including the valve and its extension section, volute, PT, and draft tube, during the load rejection process with combined regulation of the ball valve and guide vanes for a PT unit. Both the numerical pressure and the turbulent kinetic energy evolutions inside the runner and draft tube were obtained. Compared to results from the independent guide-vane regulation method, this approach effectively reduced the maximum pressure, the highest turbulence energy at the outlet of the runner, and the turbulence intensity along the draft tube.

Based on the volume of fluid (VOF) and standard k-ε models, Zhou et al. (2019) numerically investigated the transient characteristics of a hydraulic system under load rejection conditions for two PTs sharing a common headrace tunnel for a PSPS with an upper surge tank. They obtained the output power of the unit, pressure fluctuations at the volute inlet and draft tube outlet, as well as water level changes in the surge tank. For the surge tank, both the highest and lowest water levels calculated closely matched the field-test data. Backflows formed along the sidewall due to the outflow from impedance holes, which further developed into vortices as the water level increased.

Pavesi et al. (2018) numerically analyzed the evolution of rotating stall under conditions of power reduction from full load to approximately 70% of full load, with a constant guide-vane opening in pump mode. During this process, the corresponding change in rotational speed ranged from 100% to 93% of the rated rotational speed. They obtained the frequency and time-frequency characteristics of the pressure, hydraulic torque, and flow rate. The results showed that as the rotational speed decreased, the unsteady backflows increased.

Fu et al. (2020) investigated the transient characteristics of a hydraulic system, including the volute, runner, and draft tube, during the load rejection process. Their study was based on large eddy simulation, incorporating both the hydraulic acoustic effect and a weak water compressibility model. When compared to experimental data, the maximum deviations in the calculated rotational speed, pressure fluctuations, and axial hydraulic thrust were smaller when water compressibility was considered, as opposed to when it was not.

Based on the DES model considering the weak compressibility effect of water, Wang et al. (2019) captured the complex unsteady flows inside the guide vanes during load rejection in a PSPS. They further analyzed the frequency characteristics of flow rate, torque, power and pressure using fast Fourier transform (FFT) and continuous wavelet transform, respectively. The results showed that the strong pressure fluctuations caused by the closing of the

guide vanes had a significant impact on the flow characteristics downstream of the guide vanes. The key frequencies identified were the blade frequency and the unsteady low-frequency oscillations of the vortex rope.

Based on the Reynolds-averaged Navier-Stokes (N-S) equations, the runner rotation equation, and the elastic water hammer equation for incompressible fluids, Avdyushenko et al. (2013) proposed a numerical calculation model to simulate transient processes. They studied the rotating frequency, hydraulic torque, and the evolution of pressure distribution on the runner blades under the conditions of start-up, load rejection, and output power reduction, respectively. The results showed that the proposed model exhibited high computational efficiency, and the predicted evolutions of rotational speed and hydraulic torque were in good agreement with the experimental data.

At present, the 1D method primarily focuses on the maximum pressure and rotational speed of the units during the load rejection transition process in pumped storage power stations. Additionally, 3D transient studies mainly investigate the variation trends of dynamic parameters and flow characteristics in the complex geometric components, including the valve, volute, PT, and draft tube, under load rejection conditions. The boundary conditions at the volute inlet and draft tube outlet are generally assumed to have uniform flow. However, for actual large PTs, the dimensions of the inlet and outlet are so large that the flow inside them is not perfectly uniform, which results in relatively significant computational errors. Furthermore, there is limited research on the correlation mechanisms that analyze the strong unsteady transient characteristics, flow separation, backflow in the channel, and the relationship between combined flow control measures and complex internal vortices and vortex ropes. There is also a lack of studies on the different vortex types and their evolution patterns using combined regulation of ball valves and guide vanes under load rejection conditions.

Therefore, in this study, the complex internal flow field of the entire hydraulic system of a large PT under load rejection conditions, with combined regulation of the ball valve and guide vanes, is systematically investigated. The evolution of transient pressures, vortex characteristics, and low-frequency vortex ropes are further analyzed using spectrum and vortex recognition techniques.

2. FLOW GOVERNING EQUATIONS AND NUMERICAL METHODS

2.1 Flow Governing Equations and Turbulence Models

The governing equations for turbulent incompressible flow in a hydraulic system include the mass conservation and momentum conservation equations:

$$\frac{\partial \rho}{\partial t}+\frac{\partial\left(\rho u_i\right)}{\partial x_i}=0 \quad i=1,2,3 \tag{1}$$

$$\frac{\partial\left(\rho u_i\right)}{\partial t}+\frac{\partial}{\partial x_j}\left(\rho u_i u_j\right)=-\frac{\partial p}{\partial x_i}+\frac{\partial}{\partial x_j}\left[\mu\left(\frac{\partial u_i}{\partial x_j}+\frac{\partial u_j}{\partial x_i}\right)\right]+\rho f_i \tag{2}$$

where ρ is the density, t is time, p is the transient pressure, μ is the molecular viscosity, x_i and x_j are the coordinate components, u_i and u_j are the components of the flow velocity, and f_i is the body force.

The flow inside hydraulic systems is highly complex under transient conditions. The RNG k-ε two-equation model is employed to simulate the internal flow field, taking into account large curvature, strong rotation, and high strain flow. This is because the term R, which accounts for the differences in the eddy viscosity coefficient, historical effects, and the influence of mean vorticity, is added to the ε equation based on statistical techniques. This enhancement improves calculation accuracy by incorporating vortex dynamics in turbulence. The sensitivity of the RNG k-ε model to time-varying strain rates enables it to effectively capture unsteady phenomena, meeting the accuracy requirements for the calculations. The transport equations of the RNG k-ε model are as follows (Launder & Spalding, 1972):

$$\rho\frac{\partial k}{\partial t}+\rho\frac{\partial\left(u_i k\right)}{\partial x_i}=\frac{\partial}{\partial x_j}\left[a_k(\mu+\mu_t)\frac{\partial k}{\partial x_j}\right]+G_k-\rho\varepsilon \tag{3}$$

$$\frac{\partial(\rho\varepsilon)}{\partial t}+\frac{\partial(\rho u_i\varepsilon)}{\partial x_i}=\frac{\partial}{\partial x_j}\left[a_\varepsilon(\mu+\mu_t)\frac{\partial\varepsilon}{\partial x_j}\right]+C_{\varepsilon 1}G_k\frac{\varepsilon}{k}-C_{\varepsilon 2}\rho\frac{\varepsilon^2}{k}-R \tag{4}$$

where k is the turbulent kinetic energy, defined as $k=\frac{\overline{u_i' u_i'}}{2}=\frac{1}{2}\left(\overline{u'^2}+\overline{v'^2}+\overline{w'^2}\right)$, and ε is the dissipation rate per unit volume. The model constants are: η_0=4.38, a_k=1.0, a_ε=0.769, and β=0.012. The term R is an additional correction introduced to account for the small-scale turbulence effects using Renormalization Group theory. It captures the influence of small-scale vortices, enabling the model to more accurately represent the development and dissipation processes of turbulence. The correction term R is given by: $R=\frac{C_\mu\rho\eta^3(1-\eta/\eta_0)}{1+\beta\eta^3}\frac{\varepsilon^2}{k}$, $\eta=Sk/\varepsilon$, C_μ=0.0845, where S is the modulus of the mean strain rate tensor, defined as $S=\sqrt{2S_{ij}S_{ij}}$, $S_{ij}=\frac{1}{2}(\frac{\partial u_i}{\partial x_j}+\frac{\partial u_j}{\partial x_i})$. The turbulent kinetic energy generation term G_k is given by:

$$G_k=\frac{\mu_t}{\rho}\left(\frac{\partial\overline{u_i}}{\partial x_j}+\frac{\partial\overline{u_j}}{\partial x_i}\right)\frac{\partial\overline{u_i}}{\partial x_j} \tag{5}$$

The eddy viscosity μ_t is determined by Eq. (6) for high Reynolds number and by Eq. (7) for low Reynolds number:

$$\mu_t=\rho C_\mu k^2/\varepsilon \tag{6}$$

$$\begin{cases}\mathrm{d}\left(\frac{\rho k^2}{\sqrt{\varepsilon\mu}}\right)=1.72\frac{\hat{\mu}}{\sqrt{\hat{\mu}^3-1+C_V}}\mathrm{d}\,\hat{\mu}\\ \hat{\mu}=\frac{\mu+\mu_t}{\mu}\end{cases} \tag{7}$$

2.2 Mesh Motion Models

Under load rejection conditions, where combined regulation of the ball valve and guide vanes is applied, three

types of rigid body motion are considered. The SM model is used to simulate both the runner rotation and ball valve closure based on the Multiple Reference Frame (MRF) model, while a dynamic mesh (DM) model is employed to capture the motion of the closing guide vanes.

2.2.1 MRF Model

The MRF model is a computational approach for simulating flow in rotating subdomains including the runner and the ball valve. A suitable dynamic reference frame is selected to model the rotating components, and the computational domain is divided into multiple subdomains. Each moving subdomain is assigned a dynamic reference frame corresponding to its rotational speed. At the interface between stationary and moving regions, a local reference frame transformation is applied to the variables, ensuring compatibility with adjacent domains through the sliding mesh model.

2.2.2 Sliding Mesh Model

The SM model is used to simulate the relative motion (including translation and rotation) between different regions and provides a high level of accuracy. As a moving region model, the SM model involves mesh boundaries that move rigidly relative to each other, such as through translation or rotation. In this study, the SM model is employed to simulate the rotation of the runner and the closing process of the ball valve under unsteady conditions.

2.2.3 Dynamic Mesh Model

The DM model allows for mesh boundary deformation, such as node displacement, node merging, or node addition, resulting from movement. The velocity of the moving boundary must be predefined, either as a constant or as a function, since the motion of the moving components is known. The DM model is employed to simulate the guide-vane closing process in the PSPS. Mesh motion is handled through three methods: smoothing, dynamic layering, and remeshing, as implemented in the ANSYS Fluent platform.

2.3 Vortex Identification Method

Identifying and visualizing complex vortex structures within PTs is crucial for analyzing the composition, evolution, and loss characteristics of transient flow fields.

The vortex structure invariant criterion is a commonly used method for identifying coherent vortex structures. Galilean invariants, derived from the velocity gradient tensor ∇u transformation, are employed for vortex recognition. The three matrix invariants, i.e. Galilean invariants, are denoted as *X, Y* and *Z*, and are expressed as follows:

$$X = -\mathrm{tr}\left(\nabla u\right) \tag{8}$$

$$Y = \frac{1}{2}\left\{\mathrm{tr}\left(\nabla u\right)^2 - \mathrm{tr}\left[\left(\nabla u\right)^2\right]\right\} \tag{9}$$

$$Z = -\det\left(\nabla u\right) \tag{10}$$

where tr is the trace of the matrix; det is the value of the determinant of the matrix.

Based on the above analyses, three main methods, namely Q, Δ and λ_2 criteria, are commonly used to identify vortices. By eliminating most of the shear-layer effect, the velocity gradient tensor is decomposed into a symmetric tensor *S* and an antisymmetric tensor Ω, i.e. the rotation rate tensor:

$$\nabla u = \begin{pmatrix} \frac{\partial u_x}{\partial x} & \frac{\partial u_x}{\partial y} & \frac{\partial u_x}{\partial z} \\ \frac{\partial u_y}{\partial x} & \frac{\partial u_y}{\partial y} & \frac{\partial u_y}{\partial z} \\ \frac{\partial u_z}{\partial x} & \frac{\partial u_z}{\partial y} & \frac{\partial u_z}{\partial z} \end{pmatrix}, \quad \left(\nabla u\right)^T = \begin{pmatrix} \frac{\partial u_x}{\partial x} & \frac{\partial u_y}{\partial x} & \frac{\partial u_z}{\partial x} \\ \frac{\partial u_x}{\partial y} & \frac{\partial u_y}{\partial y} & \frac{\partial u_z}{\partial y} \\ \frac{\partial u_x}{\partial z} & \frac{\partial u_y}{\partial z} & \frac{\partial u_z}{\partial z} \end{pmatrix} \tag{11}$$

$$\Omega = \frac{\nabla u - \left(\nabla u\right)^T}{2} = \frac{1}{2}\begin{pmatrix} 0 & \frac{\partial u_x}{\partial y} - \frac{\partial u_y}{\partial x} & \frac{\partial u_x}{\partial z} - \frac{\partial u_z}{\partial x} \\ \frac{\partial u_y}{\partial x} - \frac{\partial u_x}{\partial y} & 0 & \frac{\partial u_y}{\partial z} - \frac{\partial u_z}{\partial y} \\ \frac{\partial u_z}{\partial x} - \frac{\partial u_x}{\partial z} & \frac{\partial u_z}{\partial y} - \frac{\partial u_y}{\partial z} & 0 \end{pmatrix} \tag{12}$$

where, $\frac{\partial u_x}{\partial x}$, $\frac{\partial u_y}{\partial y}$ and $\frac{\partial u_z}{\partial z}$ are linear strains of velocities in the three coordinate directions, respectively. The other six components are shear strains corresponding to the linear deformation and angular deformation, respectively.

$$S = \frac{\nabla u + \left(\nabla u\right)^T}{2} = \begin{pmatrix} \frac{\partial u_x}{\partial x} & \frac{1}{2}\left(\frac{\partial u_x}{\partial y} + \frac{\partial u_y}{\partial x}\right) & \frac{1}{2}\left(\frac{\partial u_x}{\partial z} + \frac{\partial u_z}{\partial x}\right) \\ \frac{1}{2}\left(\frac{\partial u_y}{\partial x} + \frac{\partial u_x}{\partial y}\right) & \frac{\partial u_y}{\partial y} & \frac{1}{2}\left(\frac{\partial u_y}{\partial z} + \frac{\partial u_z}{\partial y}\right) \\ \frac{1}{2}\left(\frac{\partial u_z}{\partial x} + \frac{\partial u_x}{\partial z}\right) & \frac{1}{2}\left(\frac{\partial u_z}{\partial y} + \frac{\partial u_y}{\partial z}\right) & \frac{\partial u_z}{\partial z} \end{pmatrix} \tag{13}$$

The Q criterion is used to identify vortices by the invariant *Y*,

$$Y = \frac{1}{2}\left[\left|\Omega\right|^2 - \left|S\right|^2\right] > 0 \tag{14}$$

The rotational module is greater than the strain module (i.e. $Q > 0$), which ensures the existence of vortex structures and maintains the vortex surface undeformed.

3. HYDRAULIC SYSTEM AND PARAMETERS OF PSPS

3.1 Pump-Turbine Hydraulic System

The pump-turbine hydraulic system primarily consists of an upper reservoir, a pressure pipeline, a ball valve, a pump-turbine unit, a tailrace pipeline, and a downstream reservoir, as shown in Fig. 1. The main parameters of the pump-turbine unit are listed in Table 1.

Table 1 Main parameters of pump-turbine unit

Parameter	Value	Parameter	Value
Rated power/MW	306.12	Flywheel moment of unit GD^2/ ($t.m^2$)	9454
Rated rotating speed/(r/min)	333.3	Number of blade	9
Rated flow rate/(m^3/s)	80.1	Number of guide vane	20
Runner diameter/m	4.565	Initial relative ball-valve opening/%	100
Rated head/m	308	Initial relative guide-vane opening/%	100

Table 2 Parameters for mesh independence test

Case	1	2	3	4
Element number/×10^6	0.9	1.9	4.0	7.8
Element type	Tetrahedron			
Element size/mm	22.825	20.54	18.26	13.695
Growth rate in boundary layer mesh	1.2	1.2	1.2	1.2
***y*+ range in boundary layer mesh**	30-70	30-70	30-70	30-70

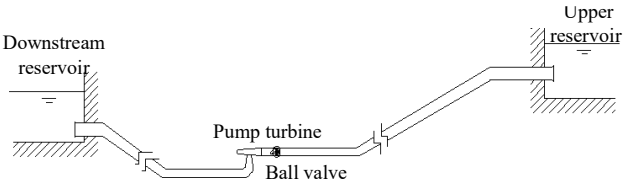

Fig.1 Schematic layout of pump-turbine hydraulic system

3.2 Mesh Layout

A total pressure is specified for the inlet condition of the upstream reservoir, with a constant water level of 330 m. This condition is convenient for calculating the load rejection transient process, where the velocity head reaches its maximum value under stable operating conditions, which is 0.129 m, only 0.039% of the total pressure head. Therefore, this type of inlet condition helps reduce parameter complexity and, to some extent, enhances computational stability. A static pressure of 0 m is adopted for the outlet condition of the downstream reservoir, which minimizes fluctuations and errors in numerical calculations, thereby improving convergence and stability. The non-slip boundary condition with the standard wall function is applied to model the flow near the wall area. The central difference scheme is used for the diffusion term, the second-order upwind scheme is applied for the convection term, and the second-order implicit method is used for the time-dependent term. The SIMPLEC algorithm is employed for velocity-pressure coupling to solve the discretized governing equations. The time step is set at 0.0005 s, and the residual convergence criterion is set at 0.0001.

The mesh layout of the computational domain for the entire flow passage, based on ICEM software, is as follows: block structures are employed to improve mesh quality and reduce the overall mesh count. Unstructured meshes are used throughout the computational domain, with refined mesh resolutions in the runner, guide vanes, and volute to capture the detailed flow field. Additionally, meshes near the wall are refined to account for boundary layer flow. All mesh qualities are greater than 0.4, which meets the requirements for numerical calculations. To study the impact of adjustable guide vane closure on the internal flow field, the elastic mesh smoothing method is applied. This method smooths the mesh through 20 iterations based on the Laplacian technique. Furthermore, the mesh reconstruction method is used to implement dynamic meshing, with a topology-based re-meshing technique that effectively handles mesh deformation when the aspect ratio exceeds 35:1.

The four mesh schemes of 0.9×10^6, 1.9×10^6, 4×10^6 and 7.8×10^6 are selected to validate the mesh-independent test under the rated operating condition. The Prism Layer is used to generate orthogonal meshes near the wall surface to ensure sufficient resolution in the y-direction (normal direction). For the adopted RANS k-ε turbulence model, the refined mesh area covers the logarithmic law layer ($30 < y^+ < 100$) and the outer layer area. The wall function is used in the boundary layer treatment, which connects computational nodes in the logarithmic law layer near the wall surface with those in the outer layer. Additionally, y^+ distribution in several typical regions near the wall, including the runner, stay vanes, and guide vanes at an opening angle of 19°, is shown in Fig. 2. The boundary layer consists of a total of 5 layers, with the first layer thickness of 0.0003 m and a growth rate of 1.2. Three trial calculations are also performed with y^+ within the range of 30 to 70 for the boundary layers. The trial calculations show that changes in the near-wall grid nodes have minimal influence on the results. Relevant parameters for the four mesh schemes are listed in Table 2.

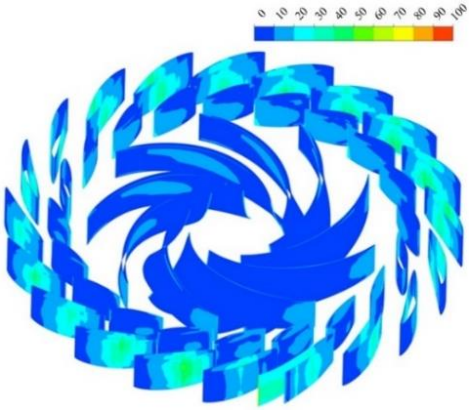

Fig. 2 *y*+ distribution in runner, stay vanes and guide vanes at opening of 19°

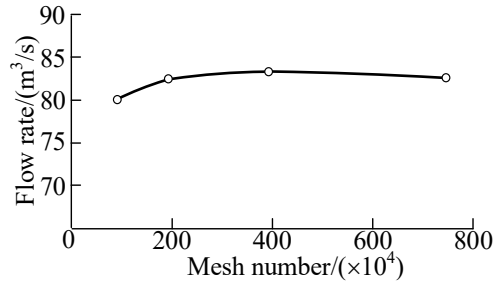

(a) Flow rate

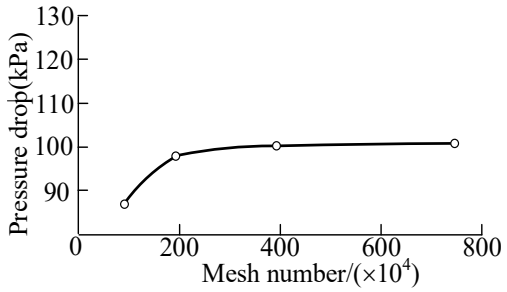

(b) Average pressure drop from stay-vane inlet to guide-vane outlet

Fig. 3 Mesh independence test

The mesh independence test of the flow rate and average pressure drop from the stay-vane inlet to the guide-vane outlet in the corresponding circumferential directions is shown in Fig. 3. For the four mesh schemes of 0.9×10^6, 1.9×10^6, 4×10^6 and 7.8×10^6, the calculated flow rates are 80.01 m³/s, 82.67 m³/s, 83.30 m³/s and 82.69 m³/s respectively, and the corresponding pressure drops from the stay-vane inlet to the guide-vane outlet are 86.01 kPa, 98.03 kPa, 100.11 kPa and 100.32 kPa respectively. The differences in flow rates and pressure drops among the latter three mesh schemes are negligible. Therefore, the mesh scheme of 4×10^6 is selected to balance computational efficiency and accuracy. The meshes for the volute, guide vanes, and runner are shown in Fig. 4.

3.3 Layout of Pressure Monitoring Points

The four sets of pressure monitoring points are arranged both in the flow direction, from the inlet of the stay vanes to the inlet of the runner, and uniformly in the circumferential direction, as shown in Fig. 5. The points P4, P16, P12, and P8 are located at the inlet of the stay vanes; the points P3, P15, P11, and P7 are positioned between the stay vanes and the guide vanes; the points P2, P14, P10, and P6 are situated in the flow passage of the guide vanes; and the points P1, P13, P9, and P5 are in the non-blade region between the runner and the guide vanes.

Additionally, the average pressure at the two monitoring points, P17 and P18, located at the volute inlet, is analyzed. A single monitoring point, P19, is positioned at the draft tube inlet on the downstream side.

3.4 On-Site Pressure Measurement Test

For the on-site test, three IMF model pressure sensors are installed at the volute inlet, at the outlet of the guide vanes near the tongue, and at the draft tube outlet, respectively. A PTIMA-20-FR-420E-M6 pull-wire

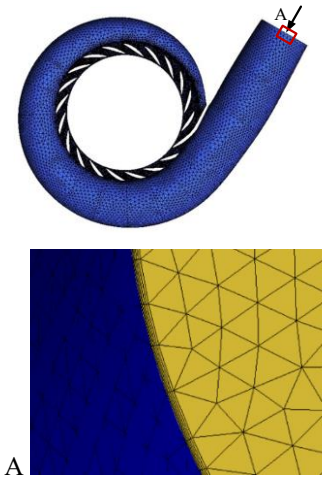

(a) Volute

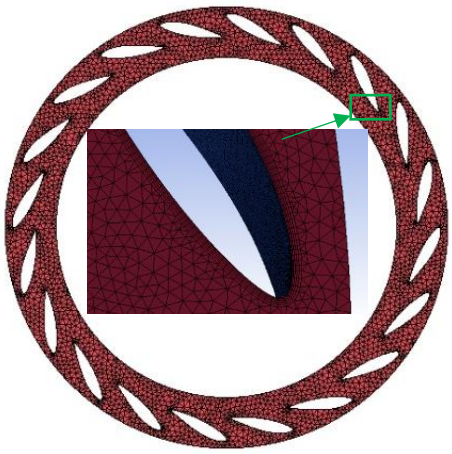

(b) Guide vanes

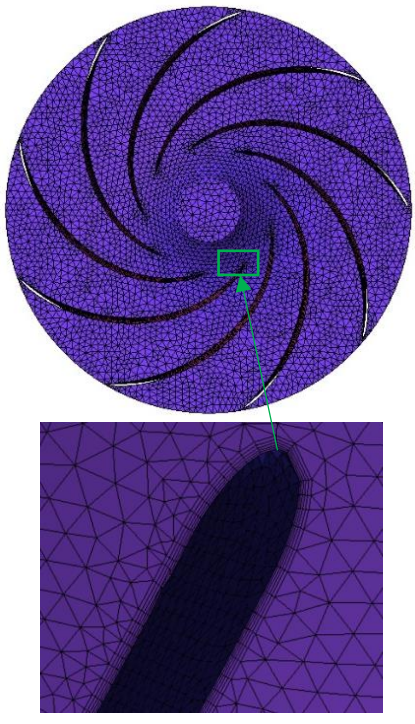

(c) Runner

Fig. 4 Meshes of volute, guide vanes and runner

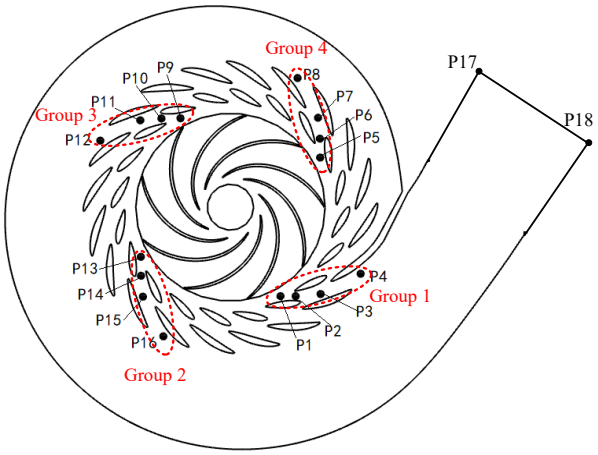

Fig. 5 Layout of pressure monitoring points in volute

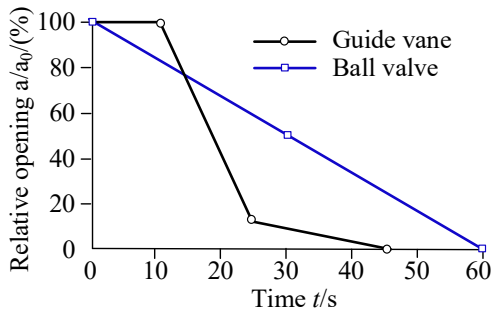

Fig. 6 Closure sequence of guide vanes and ball valve

displacement sensor is installed on the main servomotor to measure the guide-vane opening. The water head is calculated based on the pressure measured at the volute inlet and the pressure measured at the draft tube outlet.

4. TRANSIENT CHARACTERISTICS OF LOAD REJECTION UNDER TURBINE OPERATING MODE

The load rejection process of the unit, ranging from 100% to 0% of the load under rated net head, is analyzed using 3D numerical simulation results. These results are then compared with field test data.

4.1 Operation Conditions and Parameters Prior to Load Rejection

The numerical results obtained under steady-state operating conditions are used as the initial conditions for subsequent unsteady simulations of load rejection, which are conducted using a combined regulation strategy involving both the ball valve and guide vanes.

The closure sequence of the guide vanes and ball valve is illustrated in Fig. 6. During the first 60 seconds, the ball valve closes linearly from 100% to 0% of its relative opening. The guide vanes begin to close linearly at 11 seconds, reducing from 100% to 12% relative opening by 24 seconds. They then continue to close linearly from 12% to 0% relative opening, completing the closure by 35 seconds. Subsequently, the guide vanes remain fully closed at 0% relative opening. The variation in rotational speed, obtained from field test data and shown in Fig. 7, is incorporated into the simulation via a User-Defined Function (UDF) for further calculations.

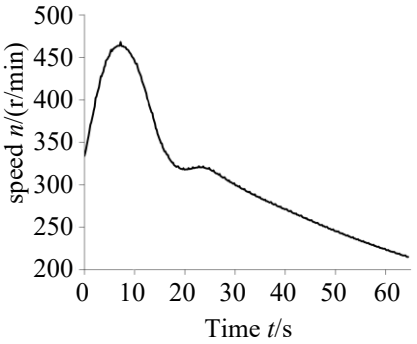

Fig. 7 Evolution of rotating speed

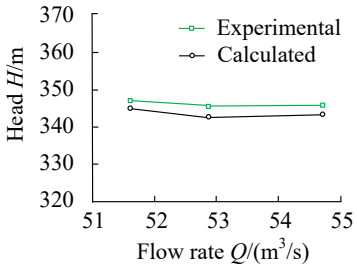

(a) guide-vane opening of 15°

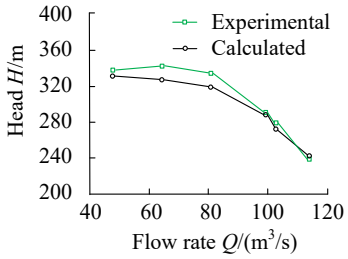

(b) guide-vane opening of 19°

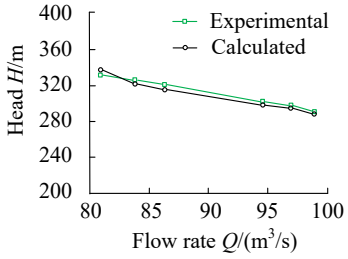

(c) guide-vane opening of 25°

Fig. 8 Head characteristic curve with flow rate under pump operating condition

To verify the accuracy of the numerical calculation method for turbulent flows inside the pump-turbine unit in the pumped storage power station, the calculated heads for three guide-vane openings of 15°, 19°, and 25° under stable operating conditions at various flow rates in pump mode are compared to the experimental data shown in Fig. 8. It can be observed that the numerical results exhibit good agreement with the experimental data across the

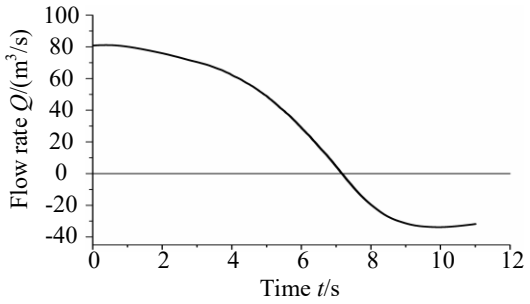

Fig. 9 Evolution of flow rate during ball valve closure (0–11 s)

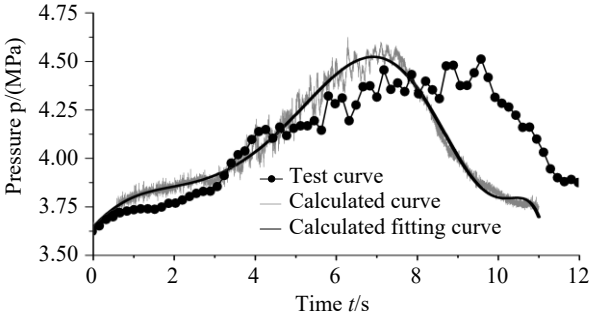

Fig. 10 Pressure vs. time at inlet of volute

three guide-vane openings. The maximum relative errors in the predicted head are 0.8%, 2.3%, and 1.8% for the guide-vane openings of 15°, 19°, and 25°, respectively. Therefore, it is verified that the relevant calculation methods are both reasonable and reliable, and the calculation results are accurate.

4.2 Analyses of Transient Flow Field During Ball Valve Closure

4.2.1 Evolution of Flow Rate

The evolution of the flow rate during the 0–11 s period, with only the ball valve closing, is shown in Fig. 9. In the first second, the flow rate changes only slightly, while the rotational speed increases rapidly due to quick load rejection. This acceleration intensifies the centrifugal force acting on the water inside the runner, leading to a sharp decrease in flow rate between 1 and 7 s. Meanwhile, as the ball valve continues to close, the flow rate keeps decreasing, and the rotational speed reaches its peak. After 7 s, the flow rate continues to drop due to the combined influence of the ball valve opening, centrifugal force, and water inertia inside the runner. Eventually, flow reversal occurs, marking the onset of reverse pump operation. Following this, the rotational speed declines, and the increase in reverse flow gradually slows.

4.2.2 Pressure and Spectrum Analyses Based on FFT

The pressure fluctuations and their corresponding spectra, based on FFT analysis, are closely related to the safety of the unit and therefore are investigated in detail.

(1) Pressure and Spectrum Analyses at Inlet of Volute

The predicted pressure at the inlet of the volute aligns well with the field test data, as shown in Fig. 10. Initially, the pressure increases and then decreases. During the 0–6 s stage, the pressure rises over time and reaches its maximum due to the centrifugal force effect caused by the increase in rotational speed. The relative error between the predicted maximum pressure of 4.62 MPa and the field test maximum of 4.58 MPa is 0.87%. Additionally, the predicted maximum occurs 2.5 seconds earlier than the field test maximum, and the overall prediction meets engineering requirements. During the 6–7 s stage, the predicted pressure is significantly higher than the on-site test pressure. After 7 s, the predicted pressure decreases rapidly, while the field test pressure begins to decrease sharply after 9 s, due to reverse flow and complex internal flow behavior. The pressure rise predicted by the model occurs earlier than observed in the experimental data. The main factors contributing to this discrepancy are as follows: During the load rejection transition process of the pump-turbine, computational results indicate that several factors may be responsible, including numerous vortices in the runner, the evolution of the draft tube vortex from thin to thick with increased pitch and fragmentation, a sharp increase in flow rate change gradient, a rise in speed, and the limitations of the isotropic turbulence model, which fails to account for fluid compressibility and the associated pressure acoustic wave magnitude. These combined effects result in an earlier predicted occurrence of maximum pressure at the volute inlet compared to experimental results. The specific causes are detailed below.

① During the load rejection transition, the numerous vortices within the flow passage cannot be fully captured by the isotropic turbulence model, particularly in terms of the energy transfer delay between vortices. This discrepancy alters the effective pressure wave velocity of the fluid, advances the pressure wave propagation phase, and consequently leads to the premature prediction of pressure peaks.

② The predicted steeper flow rate change gradient may induce faster variations in mass flow, thereby triggering pressure peaks earlier than expected.

③ Neglecting fluid compressibility underestimates the pressure wave velocity, resulting in an early prediction of pressure peaks.

④ The enhanced dissipation predicted by the turbulence model reduces the steepness of the pressure wave front, leading to overestimated calculations of the equivalent wave speed.

The corresponding pressure fluctuation can be obtained by subtracting the pressure from the fitted curve, as shown in Fig. 11. The maximum pressure fluctuation is 0.15 MPa, which is approximately 5% of the rated head. The pressure fluctuation exhibits significant time-dependent changes and shows varying frequency characteristics under the load rejection condition. Therefore, the corresponding frequency spectra are analyzed using FFT over three time stages: 0–3 s, 3–8 s, and 8–11 s, as shown in Fig. 12.

The rotational speed increases from 333.33 r/min to 468 r/min, corresponding to a rotational frequency range of 5.55–7.8 Hz and a blade frequency range of 50–70.2

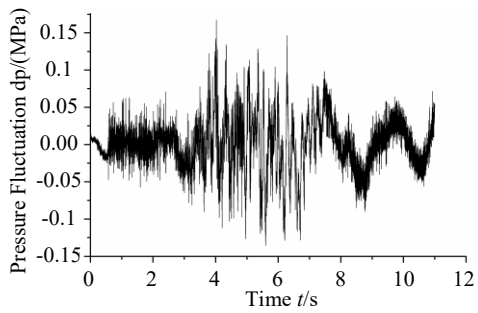

Fig. 11 Pressure fluctuation at inlet of volute

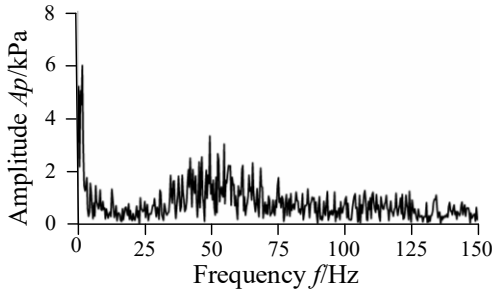

(a) 0-3s

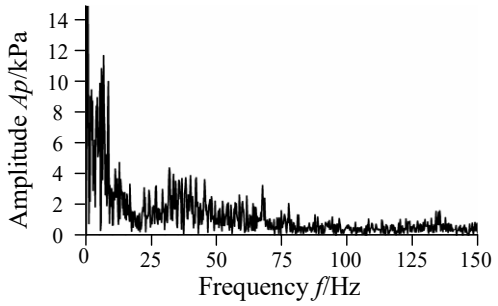

(b) 3-8 s

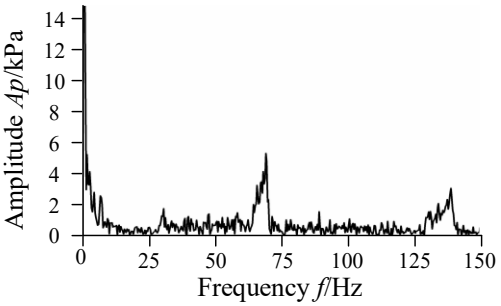

(c) 8-11s

Fig. 12 Frequency spectra of pressure fluctuations at inlet of volute

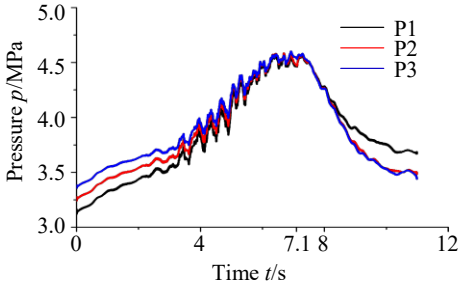

(a) Points of P1-P3

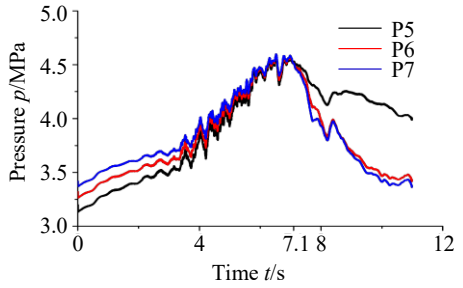

(b) Points of P5-P7

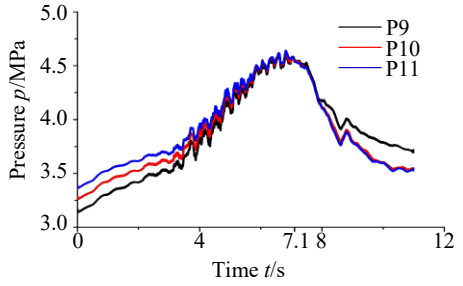

(c) Points of P9-P11

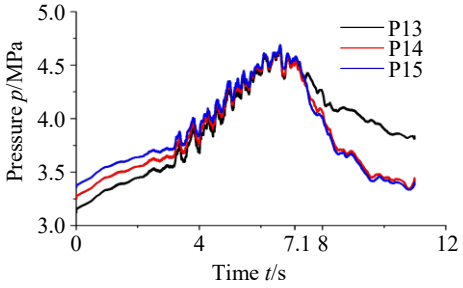

(d) Points of P13-P15

Fig. 13 Pressures at monitoring points from guide-vane inlet to vaneless area between guide vanes and runner at stage of 0-11 s

Hz. During the initial stage (0–3 s), the key frequencies are primarily composed of the rotational frequency (5.55–7.8 Hz) and the blade frequency (50 Hz) caused by the interaction between the runner and the guide vanes. At this stage (0–8 s), a small amplitude of approximately 0.006 MPa (0.2% of the rated head) is observed in the 1–3 Hz band, attributed to the low-frequency vortex rope in the draft tube. This effect diminishes and is no longer noticeable during the 8–11 s stage, as verified by the subsequent analysis of the vortex rope.

During the 3–8 s stage, the amplitudes of low-frequency fluctuations at 2 Hz, 0.5 times the blade frequency (37 Hz), and the blade frequency (67 Hz) are 0.012 MPa, 0.004 MPa, and 0.003 MPa, respectively. These fluctuations are primarily due to significant flow disturbances and pressure fluctuations at the volute inlet and in the draft tube.

In the 8–11 s stage, the low-frequency pressure fluctuation caused by the vortex rope in the draft tube dominates, with a corresponding amplitude of 15 kPa. The sub-frequency at the blade frequency (70.2 Hz) has an amplitude of 4.5 kPa, and the twice-blade frequency has an amplitude of 3.5 kPa.

(2) Pressure and Spectral Analyses in Area Between Guide Vanes and Runner

Figure 13 shows the pressures at monitoring points from the outlet of the stay vane to the outlet of the guide vane during the 0–11 s stage. During the 0–7.1 s stage, the pressure variation trends at all monitoring points are similar in turbine mode. The pressures gradually increase

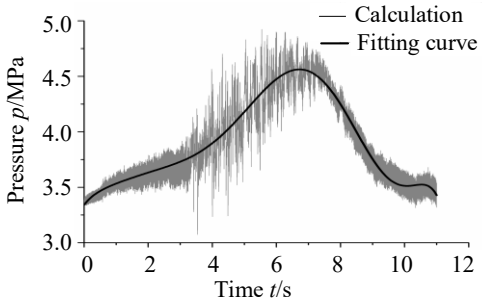

(a) Predicted result and its fitting curve

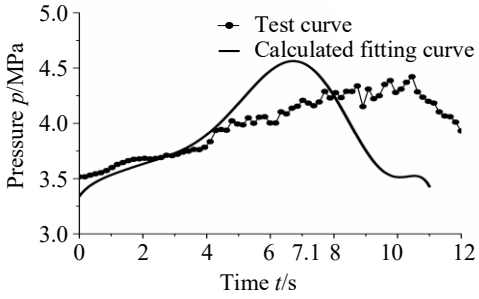

(b) Fitting curve predicted result and field test data

Fig. 14 Pressure vs. time at point P1 at stage of 0-11 s

over time, reaching their maximum at 7.1 s, and then decrease. Additionally, the pressure increases progressively along the flow direction. The pressure fluctuation amplitudes are relatively small between 0–3.6 s and relatively larger between 4–7.1 s, peaking around 4 s. After the flow rate decreases to zero at 7.1 s, the PT operates in reverse pump mode. In this phase, the pressures at all monitoring points gradually decrease over time, with pressures within the same group of monitoring points showing a decreasing trend from the guide vanes to the stay vanes. The pressures at the guide vane outlet are significantly higher than those in the guide-vane area and at the stay-vane outlet.

Since the pressure variation trends and pressure fluctuation frequencies at the 12 monitoring points are generally similar, a detailed analysis is conducted at monitoring point P1, as shown in Fig. 14. The predicted pressure closely matches the field test data. During the 0–4 s stage, the pressures increase over time, but the predicted pressure is lower than the field test data until both values converge at 4 s. Afterward, the pressures continue to increase and reach their maxima. During the 4–6.8 s stage, the predicted pressure exceeds the field test data, then decreases rapidly after 6.8 s. A short-term significant increase is observed between 4–5 s due to the large centrifugal force, while the field test data begins to decrease rapidly after 10.5 s. The relative error between the predicted maximum pressure of 4.6 MPa and the field test maximum of 4.45 MPa is 0.33%, with the predicted maximum occurring 4.2 seconds earlier than the experimental data. In addition to the earlier prediction of the maximum pressure at the volute inlet, which deviates from the experimental values, the following two factors contribute to the discrepancy:

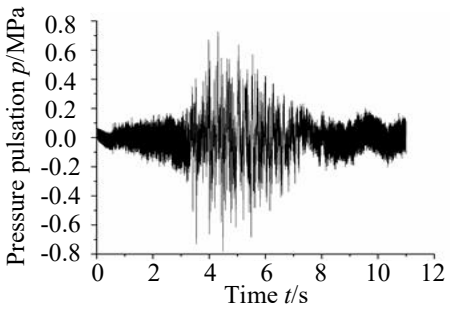

Fig. 15 Pressure pulsation at point P1 at stage of 0-11 s

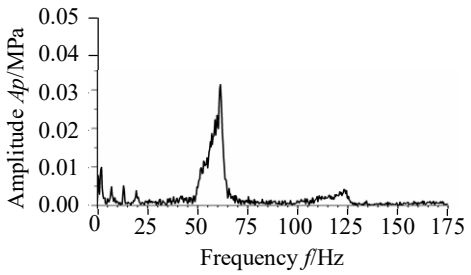

(a) 0-3 s

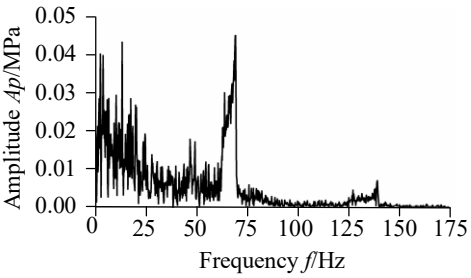

(b) 3-8 s

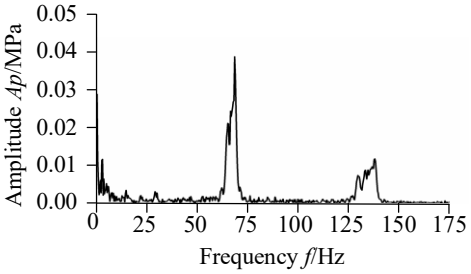

(c) 8-11 s

Fig. 16 Frequency spectrum of pressure pulsation at point P1 at three time stages

① The faster rate of rotational speed increase during certain phases may advance the occurrence of the pressure peak.

② The failure to specifically account for flow interactions between the movable guide vanes and the runner may also contribute to the premature prediction of the pressure peak.

It can be observed that the pressure fluctuation at monitoring point P1, as shown in Fig. 15, is significantly larger than that at the volute inlet, with the maximum amplitude reaching approximately 0.8 MPa. The pressure spectra for the three time periods are shown in Fig. 16. It can be seen that the dominant frequency is consistently the blade frequency, with amplitudes of 0.033 MPa during the 0–3 s stage, 0.045 MPa during the 3–8 s stage, and 0.038 MPa during the 8–11 s stage. This is followed by low-

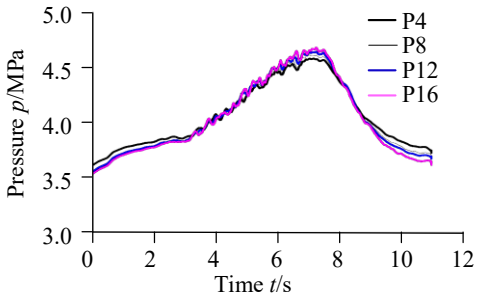

Fig. 17 Pressures in stay-vane passage

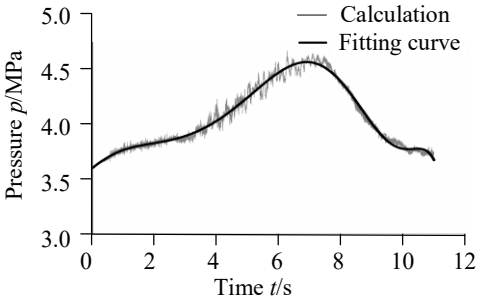

(a) Pressure and its fitting curve

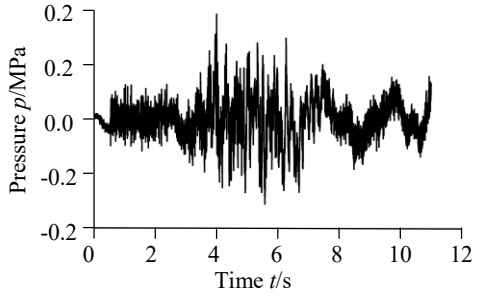

(b) Pressure pulsation

Fig. 18 Pressure and pulsation at point P4

frequency pressure pulsations, with amplitudes of 0.01 MPa during the 0–3 s stage, 0.044 MPa during the 3–8 s stage, and 0.028 MPa during the 8–11 s stage.

(3) Pressure and Spectral Analyses in Area of Stay Vanes

Figure 17 presents the pressure evolution at four monitoring points, P4, P8, P12, and P16, located in the stay vane region. The pressure trends over time are generally consistent around the circumference. However, the pressure at monitoring point P4, located near the tongue, is slightly higher than at the other three points during the 0–4 s and 8–11 s stages, but significantly lower during the 4–8 s stage.

Since the pressure variation trends and pressure fluctuation frequencies at the four monitoring points are generally similar, a detailed analysis is conducted at monitoring point P4, as shown in Fig. 18. It can be observed that the pressure increases until it reaches a maximum of 4.7 MPa at 6.8 s, after which it decreases. To account for the obvious time-dependent changes in pressure pulsation, the time is divided into four segments for spectral analysis, as shown in Fig. 19. During the 0–3 s stage, the pressure pulsation is relatively small, with the blade frequency being the dominant frequency. In the 3–6 s stage, pressure pulsations increase, with key frequencies including the unit rotational frequency (5–7.8 Hz) and the low-frequency draft tube vortex rope frequency (1–3 Hz). In the 6–8 s stage, the unit rotational frequency is the primary frequency, with the blade frequency appearing as a secondary frequency. In the 8–11 s stage, the unit rotational frequency decreases significantly due to the reduced rotational speed, and the blade frequency (65–70 Hz) becomes the dominant subfrequency.

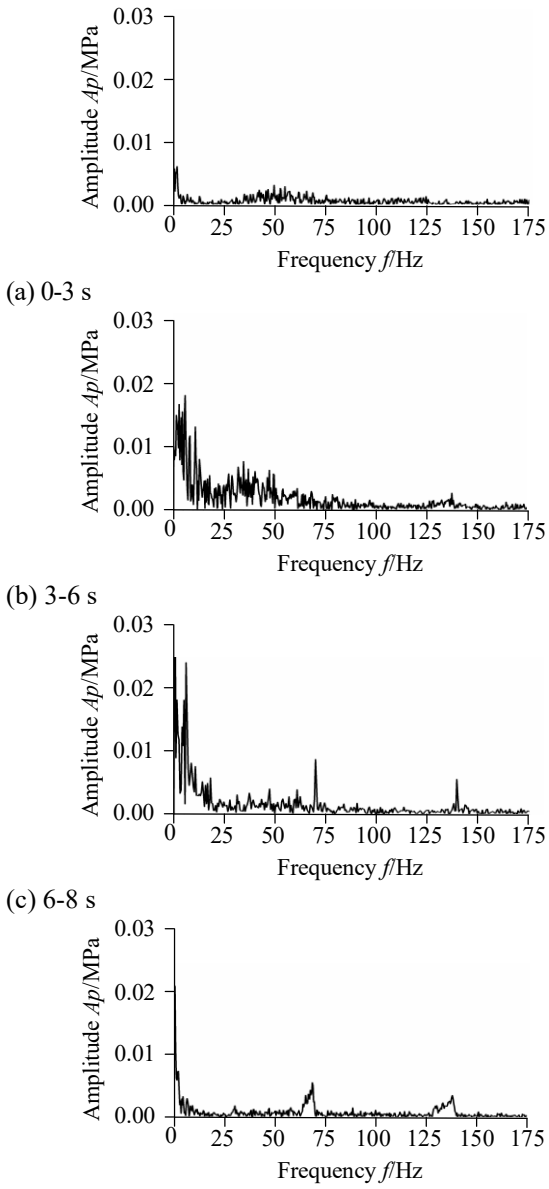

(a) 0-3 s

(b) 3-6 s

(c) 6-8 s

(d) 8-11 s

Fig. 19 Pressure pulsation spectrum at measurement point P4

4.2.3 Analyses of Transient Flow Characteristics Inside PT Unit

(1) Analyses of Flow Fields Inside Volute

The pressure distributions inside the volute show that the pressure gradient increases during the 0–10 s stage, as shown in Fig. 20. During the 0–2 s stage, the distributions

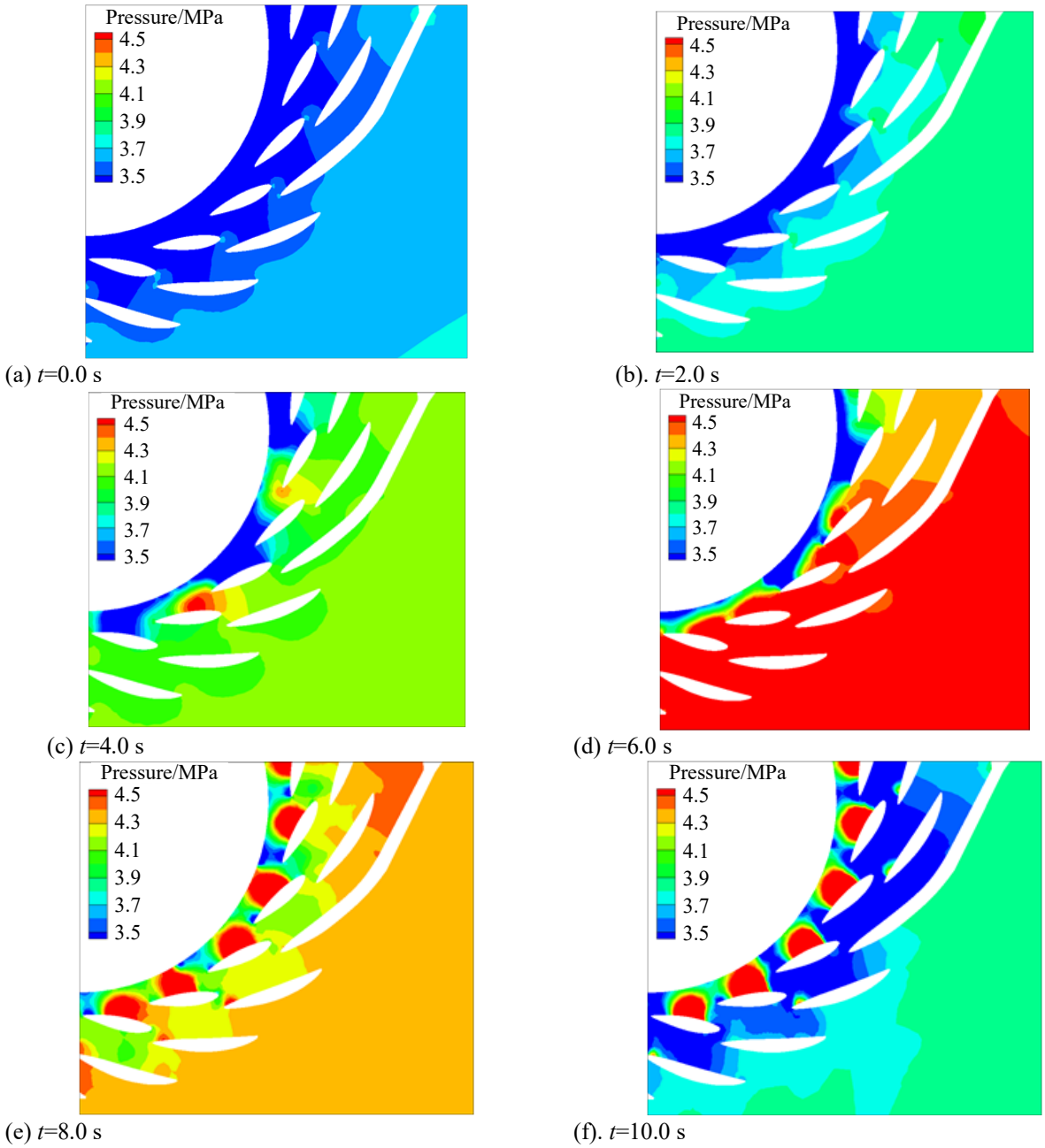

(a) t=0.0 s (b). t=2.0 s

(c) t=4.0 s (d) t=6.0 s

(e) t=8.0 s (f). t=10.0 s

Fig. 20 Pressure contours near tongue during 0-10 s

are relatively uniform and smooth, while they become disordered in the 4–10 s stage.

At 0 s, the pressure distribution is uniform along the circumferential direction and increases radially. The pressure in the flow passage ranges from 3.5 MPa at the guide-vane outlet to 3.8 MPa at the stay-vane inlet.

At 2 s, the pressure distribution along the circumferential direction inside the volute remains relatively uniform. The pressure in the flow passage ranges from 3.5 MPa at the guide-vane outlet to 4.1 MPa at the stay-vane inlet. The pressure inside the volute increases, particularly near the monitoring points in group 4, where the maximum pressure is about 4.2 MPa.

At 4 s, the pressure inside the volute continues to rise and becomes uneven. In the bladeless area between the guide-vane outlet and the runner inlet, the pressure is approximately 4.2 MPa, while the maximum pressure is around 4.5 MPa near the monitoring points in group 1 and 4.4 MPa near group 4.

At 6 s, the pressure inside the volute further increases to about 4.5 MPa, with the high-pressure area expanding to cover almost the entire volute and guide-vane regions. The pressure distribution in the vaneless area between the guide vanes and the runner becomes non-uniform along the circumference, with a significant pressure gradient along the radial direction.

At 8 s, the pressure in the vaneless area of the volute begins to decrease, dropping to around 4.4 MPa. The maximum pressure is 4.5 MPa near the middle of the guide-vane pressure sides. The pressure at the guide-vane outlet exceeds that at the volute inlet, causing the PT to operate in reverse pump mode, leading to complex flow within the volute.

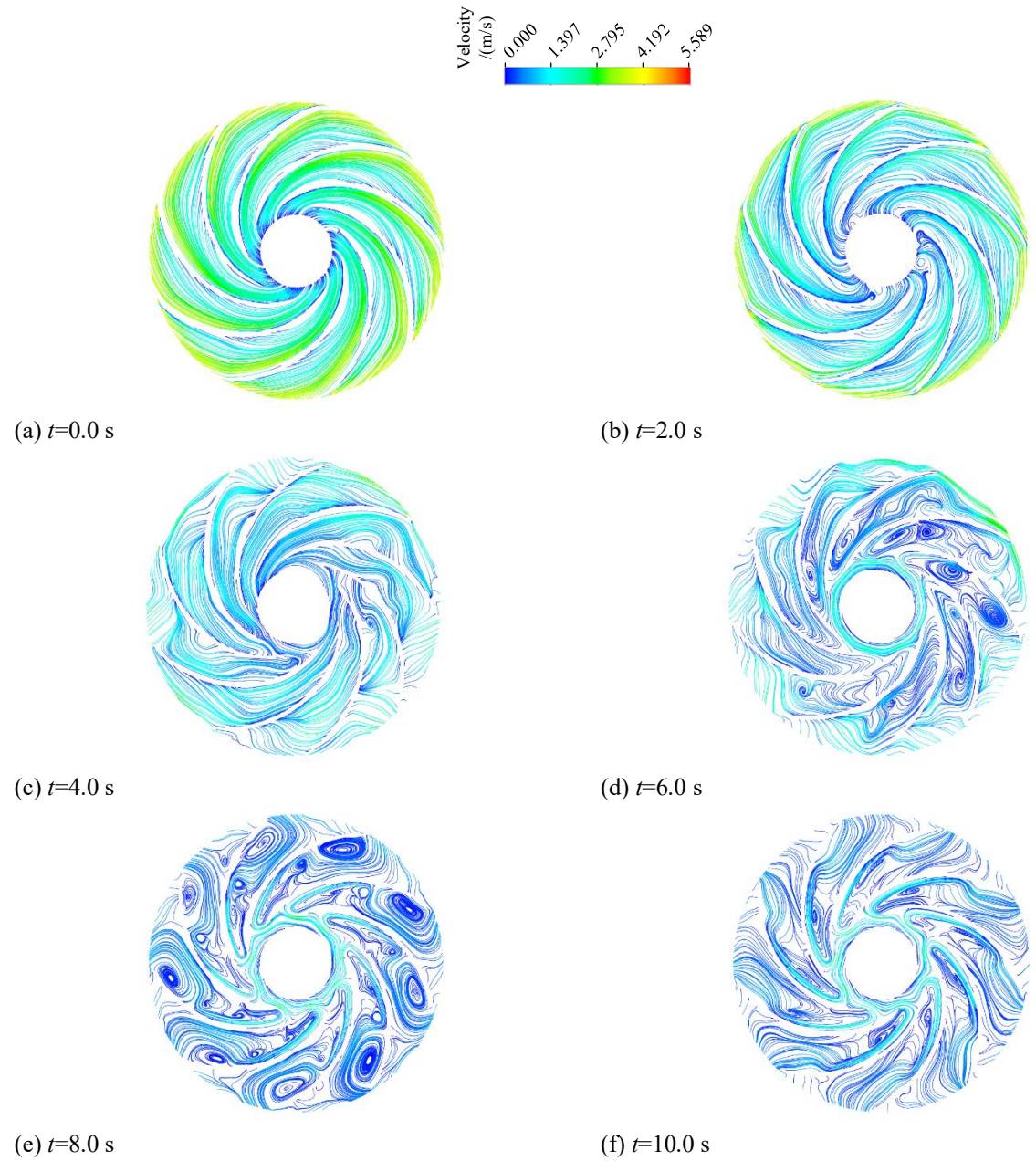

(a) t=0.0 s (b) t=2.0 s

(c) t=4.0 s (d) t=6.0 s

(e) t=8.0 s (f) t=10.0 s

Fig. 21 Evolutions of streamlines inside runner during 0-11 s stage of load rejection

At 10 s, the pressure near the middle of the guide-vane pressure sides remains relatively unchanged, while the pressure in other areas decreases further to around 3.5 MPa, especially in the vaneless area between the stay vanes and the guide vanes.

(2) Analyses of Flow Fields Inside Runner

Figure 21 illustrates the streamline distribution inside the runner during load rejection. At 0 s, the flow within the runner passes smoothly through the blade passages without flow separation, and the relative velocity increases from the pressure side to the suction side of the blades. At 2 s, as the unit's rotational speed increases, the relative velocity inside the runner also rises, while the relative velocity flow angle decreases, resulting in a small positive attack angle at the blade inlet. At the same time, small flow separations appear near the blade outlet.

As the rotational speed continues to rise and the flow rate decreases, the relative velocity flow angle further decreases. The corresponding increase in the positive attack angle alters the flow direction, gradually leading to flow separation within the passages. At 4 s, vortices form near the middle of the runner, inducing lateral flow in the mainstream within each runner passage. This effect is particularly pronounced near the tongue, where the flow becomes more disordered, further obstructing the passage toward the runner outlet and causing a significant decrease in flow rate.

At 6 s, the rotational speed increases further, and the flow inside the runner becomes asymmetric. The positive attack angle at the runner inlet not only increases but also becomes unevenly distributed. Two large vortices of similar size and opposite rotation direction develop, further impeding the flow through the passages, particularly those near the tongue, which become completely

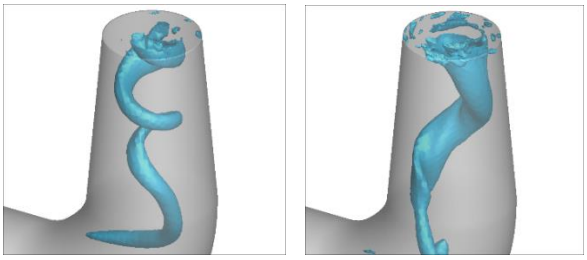

(a) t=2 s (b) t=3 s

(c) t=4 s (d) t=5 s

Fig. 22 Evolution of vortex rope in draft tube

blocked. Meanwhile, reverse flow occurs in some passages where the pressure at the runner outlet exceeds that at the inlet.

As the ball-valve opening continues to decrease and the rotational speed increases, the separation vortex grows larger until the maximum rotational speed is reached. At 8 s, noticeable reverse flows occur due to the difference in total pressures between the outlet and inlet, along with the centrifugal force, indicating that the unit is operating in reverse pump mode.

With the rapid decrease in rotational speed, the vortex size gradually increases near the runner inlet and decreases near the runner outlet until 10 s. At this point, based on the previous analysis, it can be inferred that the unit enters the unstable "S" region of the full characteristic curve of the PT. The centrifugal effect diminishes, leading to a reduction in vortex sizes within the runner. Meanwhile, the reverse flow rate increases because the difference between the total pressures at the outlet and inlet of the runner becomes more pronounced compared to the situation at 8 s.

(3) Analyses of Flow Characteristics Inside Draft Tube

When the Q-criterion is used to identify the vortex rope in the draft tube of the pump turbine, an iso-value of 0.05 is selected for Q. Figure 22 illustrates the evolution of the vortex rope in the draft tube during the 2–5 s stage.

As shown in Figs 7, 9, 15 and 22, during the process of closing the ball valve, with the decrease in flow rate, reduction in load, and increase in rotational speed, the circumferential velocity component of the water flow at the runner outlet gradually increases. As a result, by 2 s, a spiral vortex rope has formed at the inlet of the draft tube, and the pressure pulsation at the outlet of the guide vanes gradually intensifies. By 3 s, the flow rate further decreases to about 85% of Q_r, the vortex rope's cross-section becomes thicker, and its pitch increases. Simultaneously, pressure pulsation at the outlet of the guide vanes rises rapidly. By 4 s, the flow rate drops further to about 75% of Q_r, and the rate of change in flow becomes steeper, leading to significant fluctuations in pressure pulsations at the outlet of the guide vanes. The vortex rope becomes even thicker at the draft tube elbow and eventually breaks.

Therefore, during the load rejection transient process, the evolution of complex vortex ropes in the draft tube, along with intense pressure pulsations around the runner inlet, can induce unstable forces on the hydraulic turbine unit. This may result in the unit's swing amplitude exceeding the allowable limit, potentially leading to the unit lifting.

4.3 Analyses of Transient Flow Field during Combined Regulation of Ball Valve and Guide Vanes

4.3.1 Analyses of Pressure Distribution Inside Ball Valve and Volute

At 11 s, the guide vanes are activated and gradually closed from full opening, marking the beginning of combined regulation. The pressure distribution at 13 s is shown in Fig. 23a. It can be observed that the pressure downstream of the ball valve, after throttling, is significantly lower than the pressure inside the volute and upstream of the ball valve. This indicates that the ball valve continues to play a primary regulating role.

As the regulation process progresses, Fig. 23a–Fig. 23f show that the regulating effect of the guide vanes intensifies, while the regulating effect of the ball valve gradually decreases. This results in a gradual increase in pressure near the volute inlet and inside the ball valve. At 18 s, the ball valve's regulating effect becomes secondary, and the guide vanes dominate the regulation. Meanwhile, the pressure in front of the guide vanes is slightly lower, and the pressure behind them is even lower due to the throttling effect of the guide vanes.

At 21 s, the ball valve plays a minimal throttling role, with the flow being primarily regulated by the guide vanes. At this point, there is little difference in pressure from the ball valve to the inlet of the guide vanes. The pressure at the guide vane outlet is approximately 3.2 MPa, while the pressure at the runner inlet is around 1.9 MPa. Notably, the throttling effect in the vaneless area near the outlet of the guide vane is quite pronounced.

4.3.2 Analyses of Vortex Structure Based on Q Criterion

(1) Analyses of vortex structure inside volute and ball valve

Figure 24 shows the evolution of the 3D vortex structures inside the volute and ball valve, obtained using the vortex recognition method based on the Q criterion, during the combined rejection stage.

The throttling effect caused by the closing of the ball valve generates submerged jets, which lead to the formation of a series of vortices inside and downstream of the valve. During the evolution of the coherent vortices in the water flow, the vortex structures are influenced by the spiral boundary of the volute and the vane boundaries. This causes the large, coherent vortex structures to break

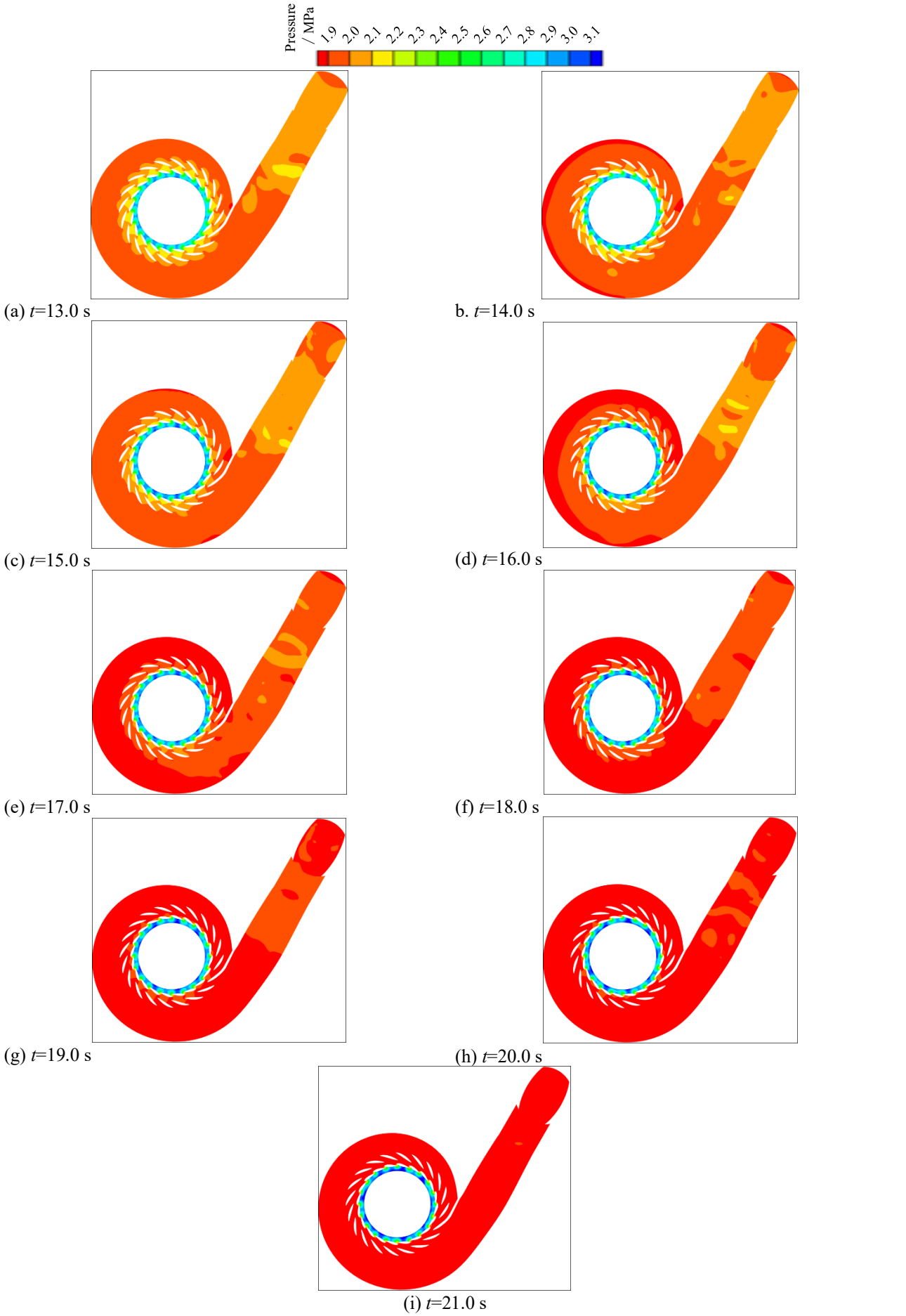

Fig. 23 Pressure evolutions inside ball valve and volute during combined regulation of ball valve and guide vanes

(a) t=13.0 s

(b) t=14.0 s

(c) t=15.0 s

(d) t=16.0 s

(e) t=17.0 s

(f) t=18.0 s

(g) t=19.0 s

(h) t=20.0 s

(i) t=21.0 s

Fig. 24 Evolution of 3D vortex structure inside volute and ball valve

up, with the corresponding vortex scales gradually decreasing, while smaller vortices form.

The vortex structures emerge due to the combined action of the ball valve and the guide vanes after the guide vanes begin to close at 11 s. The 3D vortex structures at 13 seconds, shown in Fig. 24a, reveal that a large number of vortices are primarily located inside the ball valve and in the pipe section near the volute inlet. As the guide vanes continue to close, the throttling effects intensify. Between 14 and 17 s, the vortices evolve and extend into the volute, spreading along the circumferential direction of the volute inlet to 180°, which accounts for approximately 52% of the volute wrap angle.

At the stage of 18-20 s, as both the valve and guide vanes continue to close, the throttling effect of the guide vanes becomes dominant. The flow rate decreases further, and the pressure upstream of the guide vanes rises significantly. Meanwhile, more vortices form downstream of the guide vanes, and the corresponding structures become more complex. The sizes of the vortex structures in the region between the ball valve and the guide vanes decrease accordingly. Under the combined action of the ball valve throttling effect, the vortex sizes throughout the region gradually shrink, especially upstream of the guide vanes. By 21 s, the vortex structures upstream of the guide vanes nearly disappear. The jet effect becomes significantly stronger due to the small guide vane opening, resulting in a series of vortices forming in the area between the runner inlet and the guide vane outlet. As the openings of both the ball valve and the guide vanes reduce, the flow rate continues to decrease, and the vortex structures inside the valve and at the volute inlet become progressively smaller.

The evolution of the vortex structure described above can be further analyzed by combining the 2D internal vortex structure and pressure evolution inside the volute. The 2D evolutions of the vortex structure and pressure distribution at the z = 0 m plane are shown in Fig. 25.

It can be observed that during the initial stage of the combined closing of the ball valve and guide vanes, between 13–17 s, the ball valve remains relatively open. In this period, the vortex structures in the region with a large pressure gradient, particularly between the stay vanes and the ball valve, are pronounced. This is especially noticeable in the section downstream of the ball valve, where the correlation between vortices and the pressure gradient is clearly evident. As the openings of both the guide vanes and the ball valve decrease further, the pressure gradient diminishes, and the number of large vortices also gradually reduces.

(2) Analyses of Vortex Structure Inside Draft Tube

As observed from the evolution of the vortex rope in the draft tube during the combined regulation stage from 13 to 21 s, shown in Fig. 26, the flow rate gradually decreases and deviates from the design operating conditions. From the velocity triangle at the outlet of the runner, it can be seen that the water flow no longer exits the runner in the normal direction. Instead, the circumferential velocity component increases, generating a strong swirling flow and forming a spiral vortex rope that rotates around its own central axis, referred to as “self-rotation.” Meanwhile, the non-uniformity of the water flow at the outlet of the runner intensifies, and the pressure field distribution becomes uneven. Consequently, the

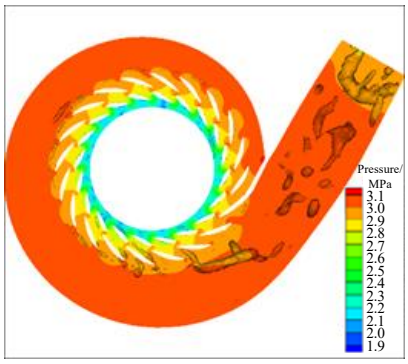

(a) t=13.0 s

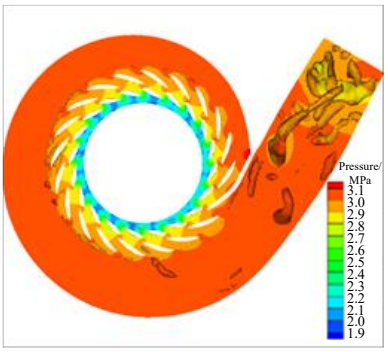

(b) t=14.0 s

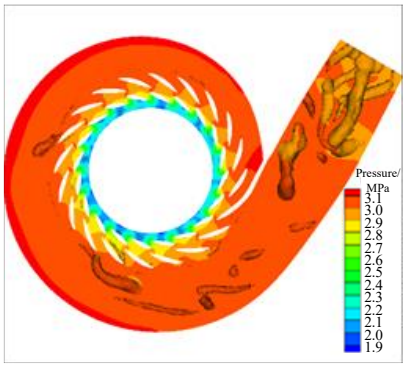

(c) t=15.0 s

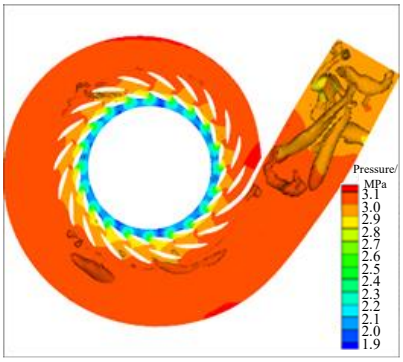

(d) t=16.0 s

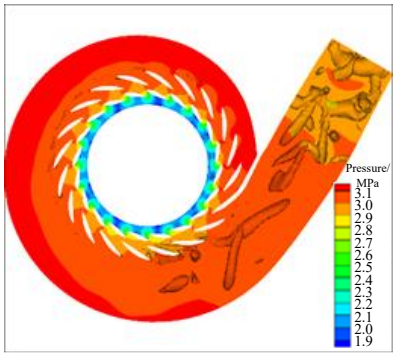

(e) t=17.0 s

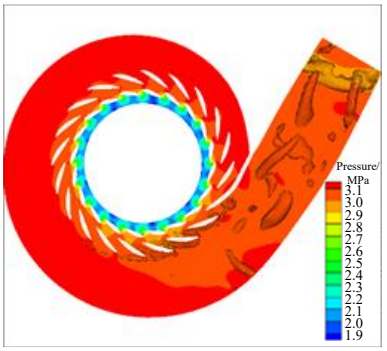

(f) t=18.0 s

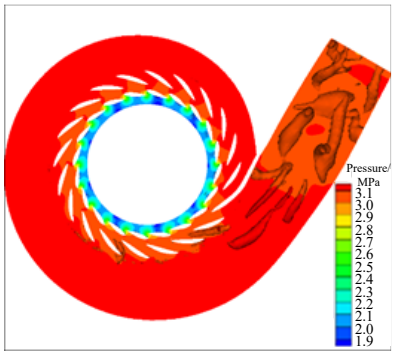

(g) t=19.0 s

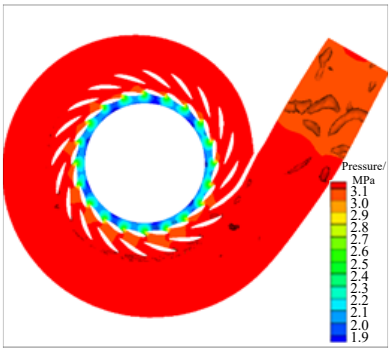

(h) t=20.0 s

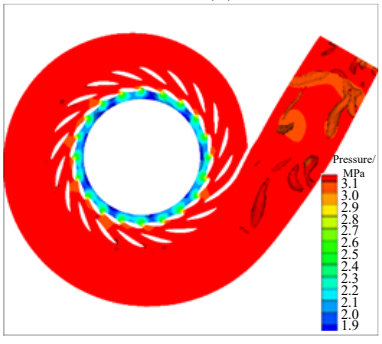

(i) t=21.0 s

Fig. 25 Evolutions of vortex structure inside volute

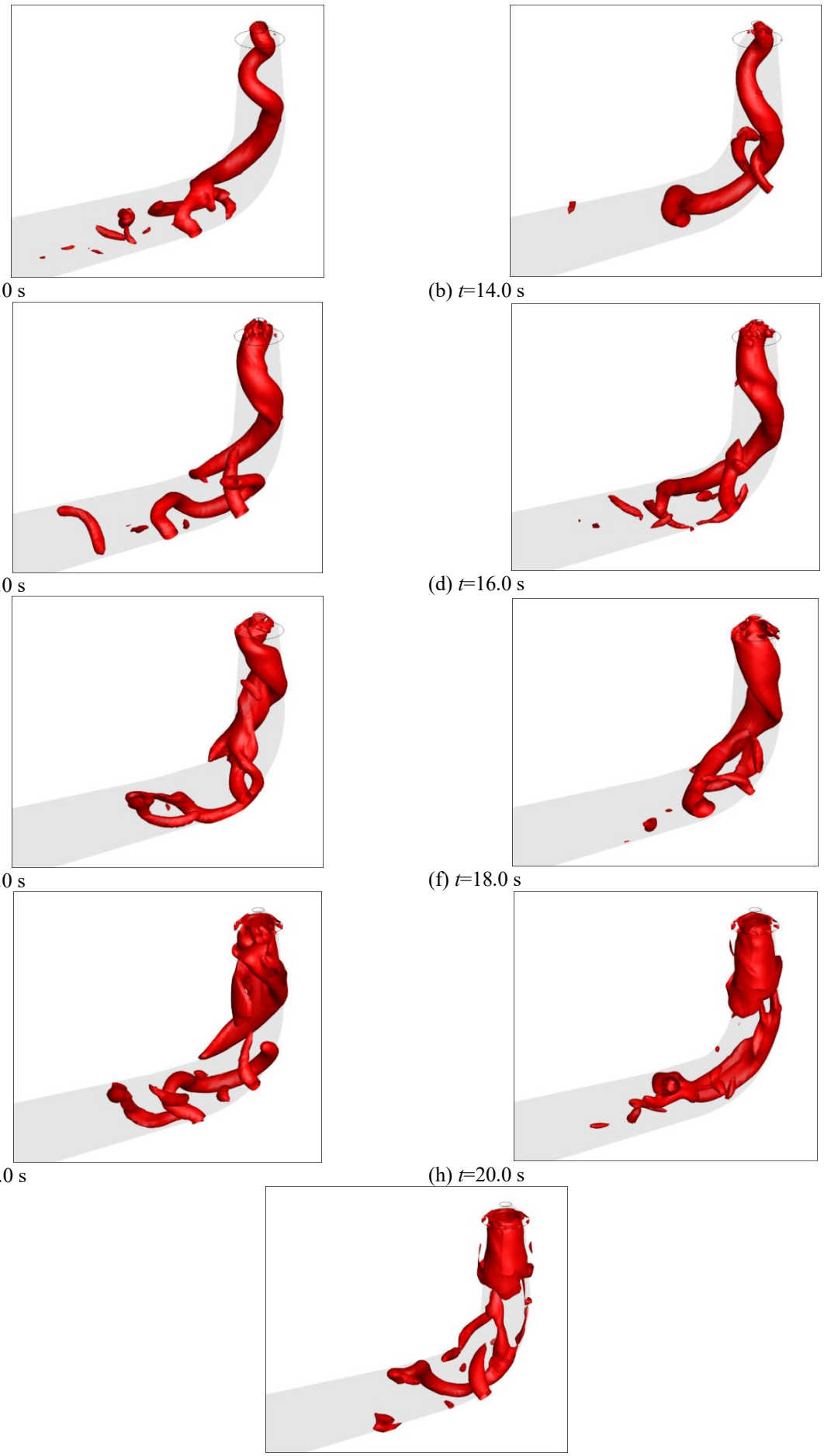

(a) t=13.0 s (b) t=14.0 s

(c) t=15.0 s (d) t=16.0 s

(e) t=17.0 s (f) t=18.0 s

(g) t=19.0 s (h) t=20.0 s

(i) t=21.0 s

Fig. 26 Evolutions of vortex rope inside draft tube during guide-vane closing process

vortex rope is subjected to periodic forces, causing it to rotate around the axis of the runner (orbital rotation). The frequency of the pressure pulsations generated by the vortex rope is approximately one-fourth of the rotational frequency. If the vortex rope's frequency is close to the natural frequency of the PT unit, it could trigger resonance in the hydroelectric generating unit, which poses a serious risk to the safe operation of the unit.

At 13 s, the spiral-shaped vortex rope in the draft tube rotates in the opposite direction to the rotation of the PT and moves downstream. After passing through the elbow of the draft tube, the vortex rope breaks into smaller vortex structures in the horizontal section of the draft tube.

As the openings of the ball valve and guide vanes decrease and the unit speed reduces, between 14 and 21 s, the relative flow velocity at the runner outlet decreases. This leads to a reduction in the frequency and pitch of the vortex rope in the draft tube, while the cross-sectional area of the vortex rope increases, and its distortion becomes more pronounced. The location of the vortex rope fracture moves upstream due to the further decrease in flow rate. Subsequently, the vortex rope breaks into relatively smaller vortex structures near the fracture site.

At 21 s, the vortex structures further break down in the straight cone section of the draft tube and are no longer in a spiral shape. During the rotation of the vortex rope in the draft tube, the vortex structures collide with the draft tube wall.

5. CONCLUSIONS

The transient characteristics of the internal flow field in the entire hydraulic system are studied in depth under the full load rejection condition for the combined regulation of the ball valve and guide vanes. The RNG k-ε model is used, while the DM technology simulates the guide vane closing process, and the SM technology simulates the runner rotation and ball valve closing process.

Firstly, the transient pressure evolutions at monitoring points located at the volute inlet, stay vanes, and guide vanes are investigated during the transient load rejection process at the stage of ball valve closing. The corresponding frequency spectra are further analyzed using the FFT technique. The predicted pressures at the volute inlet and guide-vane outlet match the field test data well, with relative errors of 0.87% and 0.33% for the predicted maximum pressures compared to the field test values, respectively. In the three individual time stages of 0–3 s, 3–8 s, and 8–11 s, the main frequencies of the pressure at the stay vane are 9n, n, and 0.4n, respectively. The main frequency at the volute inlet during the first time stage is n, while during the last two time stages, it is 0.4n. However, throughout the entire load rejection process, the main frequencies of the pressure at the guide-vane outlet are consistently 9n.

Secondly, the complex internal flow field inside the volute, runner, and draft tube is further analyzed under the load rejection condition at the ball valve closing stage. The numerical results show that the unit operates in turbine mode during the initial stage (0–6.8 s), switches to runaway mode at 6.8 s, then transitions to turbine braking mode between 6.8 and 8 s, and finally operates in reverse pump mode after 8 s. As the rotational speed increases and the flow rate decreases, the 3D flow separation in the passages becomes highly complex. Vortices form near the middle of the runner, and two large vortices, with similar sizes but opposite rotational directions, develop. The corresponding sizes of these vortices gradually increase near the runner inlet but decrease near the runner outlet. A spiral vortex rope with a regular shape, rotating at 0.4n, *is* present in the draft tube. As the flow rate decreases, the cross-sectional area and spiral shape of the vortex rope become increasingly irregular until it eventually breaks.

Finally, based on the Q criterion, the 3D vortex structures and their evolution in the ball valve, volute, and draft tube during the combined closing stage of the ball valve and guide vanes are analyzed in detail. A series of vortices form inside and downstream of the ball valve at the beginning, gradually intensifying as the guide vanes close. When the throttling effect of the guide vanes becomes dominant, more complex vortices form downstream of the guide vanes, and the vortex sizes throughout the region gradually decrease. A spiral-shaped vortex rope moves downstream in the draft tube. At approximately 85% of Q_r, the vortex rope's cross-section thickens, and its pitch increases. At about 75% Q_r, the vortex rope becomes even thicker in cross section and breaks at the draft tube elbow.

In future research, to improve the transient characteristics during the load rejection process, it will be necessary to adopt higher precision numerical methods and/or hybrid models, such as the RANS-LES model. Further comparisons can be made between different regulation schemes, and optimized combined regulation rules for the ball valve and guide vanes under the corresponding load rejection conditions can be developed. The closure scheme for the ball valve and guide vanes should be optimized based on the pressure rise rate and peak distribution obtained from transient simulations, ensuring that the pressure peaks remain within permissible design limits. Additionally, during the selection and design of the hydraulic system, computational results can be used to guide the rational optimization of water hammer protection measures to prevent accidents.

ACKNOWLEDGEMENTS

This work was supported by the National Natural Science Foundation of China (Grant Nos. 52379095，52079140).

CONFLICT OF INTEREST

The authors declare no conflict of interest.

AUTHORS CONTRIBUTION

Xiaoqin Li: Methodology, writing- original draft preparation, investigation, collecting experimental data. **Xuelin Tang:** Methodology, CFD numerical calculation

methods. **Qian Ren:** CFD calculations, analysis. **Qihang Liu:** Processing computational data and figures. **Haoyang An:** Organizing computational data.

REFERENCES

Avdyushenko, A. Y., Cherny, S. G., Chirkov, D. V., Skorospelov, V.A., & Turuk, P.A. (2013). Numerical simulation of transient processes in hydroturbines. *Thermophysics and Aeromechanics, 20(5),* 577-593. https://doi.org/10.1134/s0869864313050059

Chen, S., Wang, J., & Zhang, J. (2020). Transient behavior of two-stage load rejection for multiple units system in pumped storage plants. *Renewable Energy, 160,* 1012-1022. https://doi.org/10.1016/j.renene.2020.06.116

Chen, S., Zhang, J., Li, G., & Yu, X. (2019). Influence mechanism of geometric characteristics of water conveyance system on extreme water hammer during load rejection in pumped storage plants. *Energies, 12*(15). https://doi.org/10.3390/en12152854

Feng, C., Sun, J., Zhang, Y., & Zheng, Y. (2024). A novel multi-excitation transient vibration framework for coupling three- and one-dimensional pumped storage hydropower shafting systems. *Physics of Fluids, 36*(10). https://doi.org/10.1063/5.0229598

Fu, X., Li, D., Song, Y., Wang, H., & Wei, X. (2023). High-amplitude pressure fluctuations of a pump-turbine with large head variable ratio during the turbine load rejection process. *Science China: Technological Sciences (English), 66*(9), 2575-2585. https://doi.org/10.1007/s11431-022-2322-9

Fu, X., Li, D., Wang, H., Li, Z., Zhao, Q., & Wei, X. (2021). One- and three-dimensional coupling flow simulations of pumped-storage power stations with complex long-distance water conveyance pipeline system. *Journal of Cleaner Production, 315*, 128228 https://doi.org/10.1016/j.jclepro.2021.128228

Fu, X., Li, D., Wang, H., Zhang, G., Li, Z., & Wei, X. (2020). Numerical simulation of the transient flow in a pump-turbine during load rejection process with special emphasis on hydraulic acoustic effect. *Renewable Energy, 155,* 1127-1138. https://doi.org/10.1016/j.renene.2020.04.006

Guo, P. C., Zhang, H., & Sun, L. G. (2020). Transient dynamic analysis of a pump-turbine with hysteresis effect. *Modern Physics Letters B,* 2050125. https://doi.org/10.1142/S0217984920501250

He, X., Hu, J., Zhao, Z., Lin, J., Xiao P., Yang J., & Yang, J. (2023). Water column separation under one-after-another load rejectionin pumped storage station. *Energy. 278*, 127809. https://doi.org/10.1016/j.energy.2023.127809

Hoffstaedt, J. P., Truijen, D. P. K., Fahlbeck, J., Gans, L. H. A., Qudaih, M., Laguna, A. J., De Kooning, J. D. M., Stockman, K., Nilsson, H., Storli, P. T., Engel, B., Marence, M., & Bricker, J. D. (2022). Low-head pumped hydro storage: A review of applicable technologies for design, grid integration, control and modelling. *Renewable and Sustainable Energy Reviews, 158*, 1-16. https://doi.org/10.1016/j.rser.2022.112119

Jurasz, J., & Mikulik, J. (2017). A strategy for the photovoltaic-powered pumped storage hydroelectricity. *Energy & Environment, 28*(5), 1-20. 0958305. http://dx.doi.org/10.1177/0958305x17714174

Launder, B. E., & Spalding, D. B. (1972). *Lectures in mathematical models*. London: Academic Press.

Li, X., Tang, X., Shi, X. Chen, H., & Li, C. (2018). Load rejection transient with joint closing law of ball-valve and guide vane for two units in pumped storage power station. *Journal of Hydroinformatics, 20*(2), 301-315. https://doi.org/10.2166/hydro.2017.106

Liu, D., Zhang, X., Yang, Z. Li, Z., Zhao, Q., & Wei, X. (2021). Evaluating the pressure fluctuations during load rejection of two pump-turbines in a prototype pumped-storage system by using 1D-3D coupled simulation. *Renewable Energy, 171,* 1276-1289. https://doi.org/10.1016/j.jclepro.2021.128228

Mao, X., Chen, X., Lu, J., Liu, P., & Zhang, Z. (2022). Improving internal fluid stability of pump turbine in load rejection process by co-adjusting inlet valve and guide vane. *Journal of Energy Storage, 50,* 104623. https://doi.org/10.1016/j.est.2022.104623

Pavesi, G., Giovanna, C., & Ardizzon, G. (2018). Numerical simulation of a pump–turbine transient load following process in pump mode. *Journal of Fluids Engineering, 140*, 021114. https://doi.org/10.1115/1.4037988]

Rezghi, A., & Riasi, A. (2016). Sensitivity analysis of transient flow of two parallel pump-turbines operating at runaway. *Renewable Energy, 86,* 611-622. http://dx.doi.org/10.1016/j.renene.2015.08.059

Sharon, M. (2020). *1D and 3D water-hammer models: The energetics of high friction pipe flow and hydropower load rejection*. University of Toronto. Toronto, Canada.

Vakil, A., & Firouzabadi, B. (2009). Investigation of valve-closing law on the maximum head rise of a hydropower plant. *Scientia Iranica, 16*(3), 222-228. https://doi.org/10.1115/1.4029313

Walseth, E. C., Nielsen, T. K., & Svingen, B. (2016). Measuring the dynamic characteristics of a low specific speed pump-turbine model. *Energies, 9*(3), 1-12. https://doi.org/10.3390/en9030199

Wang, W., Giorgio, P., Pei, J. & Yuan, S. (2019). Transient simulation on closure of wicket gates in a high-head Francis-type reversible turbine operating in pump mode. *Renewable Energy, 145,* 1817-1830. https://doi.org/10.1016/j.renene.2019.07.052

Widmer, C., Staubli, T., & Ledergerber, N. (2011). Unstable characteristics and rotating stall in turbine brake operation of pump-turbines. *Journal of Fluids Engineering, 133*(4), 041101.

https://doi.org/10.1115/1.4003874

Yang, Z., Cheng, Y., Xia, L. Meng, W., Liu K., & Zhang, X. (2020). Evolutions of flow patterns and pressure fluctuations in a prototype pump-turbine during the runaway transient process after pump-trip. *Renewable Energy, 152*, 1149-1159. https://doi.org/10.1016/j.renene.2020.01.079

Yin, C., Zeng, W., & Yang, J. (2021). Transient simulation and analysis of the simultaneous load rejection process in pumped storage power stations using a 1-D-3-D coupling method. *Journal of Hydrodynamics, 33*(5), 979-991. https://doi.org/10.1007/s42241-021-0087-8

Zeng, W., Yang, J., & Guo, W. (2015). Runaway instability of pump-turbines in S-shaped regions considering water compressibility. *Journal of Fluids Engineering, 137*(5), 051401. https://doi.org/10.1115/1.4029313

Zeng, W., Yang, J., & Hu, J. (2017). Pumped storage system model and experimental investigations on S-induced issues during transients. *Mechanical Systems and Signal Processing, 90,* 350-364. http://dx.doi.org/10.1016/j.ymssp.2016.12.031

Zhang, F., Fang, M., Tao, R., Zhu, D., Liu, W., Lin, F., & Xiao, R. (2024). Chaotic analysis of the reversible pump turbine exhaust process in pump mode based on a data-driven method. *Journal of Applied Fluid Mechanics*, *17*(11), 2361-2376. https://doi.org/10.47176/jafm.17.11.2669

Zhang, H., Guo, P., & Sun, L., (2020). Transient analysis of a multi-unit pumped storage system during load rejection process. *Renewable Energy, 152*, 34-43. https://doi.org/10.1016/j.renene.2019.12.111

Zhang, X., & Cheng, Y., (2012). Simulation of hydraulic transients in hydropower systems using the 1-D-3-D coupling approach. *Journal of Hydrodynamics, 24*(4), 595-604. https://doi.org/10.1016/S1001-6058(11)60282-5

Zhang, X., Cheng, Y., Xia, L., Yang, J., & Qian, Z. (2016). Looping dynamic characteristics of a pump-turbine in the S-shaped region during runaway. *Journal of Fluids Engineering, 138*(9), 091102. https://doi.org/10.1115/1.4033297

Zheng, Y., Chen Q., Yan, D. & Liu, W. (2020). A two-stage numerical simulation framework for pumped-storage energy system. *Energy Conversion and Management, 210*, 112676. https://doi.org/10.1016/j.enconman.2020.112676

Zhou, D., Chen, Y., Chen, H., Chen, S., & Yang, C. (2019). Study of hydraulic disturbances from single-unit load rejection in a pumped-storage hydropower station with a shared water delivery system. *IEEE Access, 7,* 153382-153390. https://doi.org/10.1109/ACCESS.2019.2947301

Zhou, T., Yu, X., Zhang. J., & Xu, H. (2024). Analysis of transient pressure of pump-turbine during load rejection based on a multi-step extraction method. *Energy, 292*, 130678. https://doi.org/10.1016/j.energy.2024.130578